Electronic Supplementary Material (ESI) for Energy & Environmental Science.

Electronic Supplementary Information for

Cooperative Water Oxidation Catalysis in a Series of Trinuclear Metallosupramolecular Ruthenium Macrocycles

Valentin Kunz,[a] Joachim O. Lindner,[c] Marcus Schulze,[a] Merle I. S. Röhr,[b,c] David Schmidt,[a,b]
Roland Mitrić *,[c] and Frank Würthner *,[a,b]

a) Universität Würzburg, Institut für Organische Chemie, Am Hubland, 97074 Würzburg, Germany. E-mail: wuerthner@uni-wuerzburg.de
b) Universität Würzburg, Center for Nanosystems Chemistry (CNC), Theodor-Boveri-Weg, 97074 Würzburg, Germany.
c) Universität Würzburg, Institut für Physikalische und Theoretische Chemie, Emil-Fischer-Str. 42, 97074 Würzburg, Germany. E-mail: roland.mitric@uni-wuerzburg.de

Table of Contents

1. Materials and Methods

Materials. All chemicals and solvents, if not stated otherwise, were purchased from commercial sources and used without further purification. [Ru(bda)(dmso)$_2$], the reference complex [Ru(bda)(pic)$_2$] and the ditopic pyridine ligands were synthesized according to literature known methods.[1-3] The synthesis and characterization of **MC3** has previously been described by our group.[4] Synthetic routes for the macrocycles **MC1**, **MC2** and **MC4** can be found in the Synthesis part. Column chromatographic separations were performed on neutral aluminium oxide (MP Alumina N, Act. V, 15% w/w H_2O). For thin-layer chromatography plastic sheets precoated with aluminium oxide (Polygram ALOX N/UV254, Macherey-Nagel) were used.

NMR Spectroscopy. NMR spectra were recorded on a 400 MHz NMR spectrometer (Bruker Avance III HD 400) in deuterated solvents at 25 °C if not noted otherwise. ^{13}C NMR spectra are broadband proton decoupled. Chemical shifts are reported in parts per million (ppm, δ scale) relative to the residual solvent signal of CD_2Cl_2. The following abbreviations were used to describe peak patterns: s = singlet, d = doublet, and t = triplet.

Mass Spectrometry. MALDI-ToF mass spectra have been measured on an Autoflex II spectrometer (Bruker). The spectra were measured in the positive reflector mode using DCTB (*trans*-2-[3-(4-*tert*-butylphenyl)-2-methyl-2-propenylidene]malononitrile) as matrix. High resolution mass spectra (ESI) were recorded on an ESI micrOTOF Focus mass spectrometer (Bruker).

X-ray Crystallography. Single crystals of **MC4** were obtained from a solution in a dichloromethane/methanol/2,2,2-trifluoroethanol mixture by slowly letting the solvent evaporate under a nitrogen atmosphere. Single crystal X-ray diffraction data for **MC4** was collected at 100 K on a Bruker X8APEX-II diffractometer with a CCD area detector and multi-layer mirror monochromated MoK_α radiation. The structure was solved using direct methods, expanded with Fourier techniques and refined with the Shelx software package.[5] All non-hydrogen atoms were refined anisotropically with exception of those of the disordered 2,2,2-trifluoroethanol molecules. Hydrogen atoms were included in the structure factor calculation on geometrically idealized positions. The refinement contained residual electron density resulting from solvent molecules that could not be modeled satisfactorily. Therefore, the PLATON squeeze routine was applied to remove the respective electron density.[6] The remaining structure could be refined nicely. Crystallographic data have been deposited with the Cambridge Crystallographic Data Centre as supplementary publication no. CCDC 1554426. These data can be obtained free of charge from The Cambridge Crystallographic Data Centre via www.ccdc.ac.uk/data.request/cif.

Electrochemistry. For cyclic- and differential pulse voltammetry measurements, a BAS Cell Stand C3 (BAS Epsilon) with a three electrode single-compartment cell was used. Glassy carbon was used as working electrode and a platinum wire as counter electrode. As a reference an Ag/AgCl electrode in 3 M KCl was used and the potentials were referenced to the Normal Hydrogen Electrode (NHE) by the addition of +0.209 V. The solutions were either measured in acetonitrile/water (pH 1, acid: trifluoromethane sulfonic acid (CF_3SO_3H)) or 2,2,2-trifluoroethanol/water (pH 1) mixtures. The measurements for the Pourbaix diagrams were started in a 1:1 CH_3CN/H_2O mixture at an intial pH value of 1. The further pH values have been adjusted by the addition of NaOH solutions and measured with a pH-meter.

UV/Vis Spectroscopy. UV/Vis absorption spectra were measured on a JASCO V-770 spectrophotometer at 25 °C in 1 cm quartz cuvettes with spectroscopic grade solvents.

Spectroelectrochemistry. Spectroelectrochemical experiments in reflexion were performed in an Agilent Cary 5000 Spectrometer in combination with a home-built sample compartment consisting of a cylindrical PTFE cell with a sapphire window and an adjustable three in one electrode (6 mm platinum disc working electrode, 1 mm platinum counter and pseudo reference electrode) with a layer thickness of ~100 µm in an acetonitrile/water (pH 1, acid: CF_3SO_3H) 1:1 mixture at concentrations in the range of $5–7 \cdot 10^{-4}$ M. The potential was always referenced to the first oxidation event that was measured with differential pulse voltammetry against a Ag/AgCl reference electrode (3 M KCl) and the extinction coefficient was determined for the $[Ru^{II}|Ru^{II}|Ru^{II}]$ state using conventional UV/Vis spectroscopy at a concentration of 10^{-5} M in the same solvent mixture due to the inaccuracy of the layer thickness of the spectroelectrochemical cell.

UV/Vis Redox Titration. The catalyst solutions in CH_3CN/water 1:1 (2.0 mL, c = 0.1 mM, pH 1, acid: CF_3SO_3H) were loaded into a 1 cm quartz cuvette, and freshly dissolved cerium(IV) ammonium nitrate was titrated in increments of one equivalent to it (10 µL, c = 20 mM, per addition). After each addition the mixture was stirred for ~5 min at 20 °C before the spectrum was acquired using a diode array spectrometer (Ocean Optics Maya200Pro).

Water Oxidation Catalysis with large excess of Ce(IV). The chemically driven water oxidation reactions were performed at 20 °C in reaction vessels which were connected to pressure transducers from Honeywell (SSCDANN030PAAA5, absolute pressure, 0 to 30 psi). For each measurement 1 g (1.82 mmol) of cerium(IV) ammonium nitrate (CAN) was dissolved in 3 mL of an acetonitrile/water mixture (pH 1, acid: CF_3SO_3H, ratios varying) in the reaction vessel (V = 20.6 mL) and the catalyst solution (400 µL in acetonitrile/water mixtures) was injected to it through a septum *via* a Hamilton syringe. After the gas-evolution had ceased, 500 µL of the gas head space were taken out with a gas tight Hamilton syringe and injected into the gas chromatograph GC-2010 Plus from Shimadzu, equipped with a thermal conductivity detector (detector current 30 mA, argon as carrier gas), to determine the gas composition at the end of the reaction.

The turnover numbers (TONs) have been calculated based on the total amount of evolved oxygen during catalysis, divided by the amount of used catalyst. The amount of evolved oxygen has been determined by using pressure transducers to measure the pressure increase in the reaction vessel. Using the ideal gas law $\Delta p \cdot V = \Delta n \cdot R \cdot T$ (T = 293.15 K, V = 20.6 mL, R = 8.314 J/Kmol) this pressure difference (Δp), can be converted into the amount of molecular oxygen in moles that is generated during the reaction (Δn). The TONs have been calculated for each concentration in the concentration-dependent measurements and the highest TONs are reported in the manuscript. The turnover frequencies (TOFs) have been determined from the same concentration-dependent measurements. For each concentration the initial rate of catalysis has been determined by a linear regression through the first linear part of the oxygen evolution curve. The TOF is then determined by the slope of a linear regression of these initial rates vs. the respective catalyst amounts.

Water Oxidation Catalysis with Stoichiometric Ce(IV) Amounts. The catalysis in the presence of stoichiometric amounts of cerium(IV)ammonium nitrate was investigated monitoring the decrease of the CAN absorption at 360 nm using a JASCO V-770 UV/Vis spectrometer at 25 °C. The studies were performed in 1:1 CH_3CN/water (pH 1, acid: nitric acid (HNO_3)) solution as followed: 1.99 mL of a freshly prepared cerium(IV) ammonium nitrate (CAN) solution were mixed with 10 µL of the catalyst solution. Afterwards the cuvette was shaken and placed inside the spectrometer (~ 4 s) and the Ce(IV) absorption decay (360 nm, $\varepsilon_{360} = 760\ M^{-1}\ cm^{-1}$) was monitored for 300 s.

Stability Test. The following procedure was applied to test the stability of the macrocyclic structures after water oxidation catalysis: Each catalyst was dissolved in 1 mL 4:1 acetonitrile/water ($c = 7 \times 10^{-4}$ M, pH 1, acid: CF_3SO_3H). After the addition of 130 equivalents cerium(IV) ammonium nitrate vigorous oxygen evolution occurred (~ 33 catalytic cycles). After the oxygen evolution had ceased, the sample was reduced with ascorbic acid and analyzed by MALDI-ToF mass spectrometry (matrix = DCTB).

Kinetic Isotope Experiments. The reactions were performed in 2.0 mL of a 1:1 acetonitrile/water (H_2O or D_2O, pH1, acid: CF_3SO_3H) mixture, using CAN (*c* = 0.525 M) as a sacrificial oxidant, and the dissolved oxygen concentration was measured with a Clark-type electrode setup (Oxygraph Plus System of Hansatech Instruments Ltd) at a constant temperature of 20 °C. For each measurement 1.5 mL of a freshly prepared CAN solution (*c* = 0.7 M, pH 1 solution (H_2O or D_2O) was placed in the Clark electrode reaction chamber. After the baseline was constant, 0.5 mL of the catalyst solution (varying concentrations) were added. The D_2O used for this experiment had a purity of 99.9 %.

DFT Calculations. In order to generate initial structures for the exploration of the catalytic steps in the framework of QM/MM MD simulations, the catalyst structures were first optimized in the presence of explicit water molecules at the PBE/def2-SVP level [7, 8] of theory employing 28-electron Stuttgart-Dresden effective core potentials [9] for the ruthenium atoms.

The ensemble of catalyst structures in solution used for the calculation of UV/Vis spectra has been generated by embedding pre-optimized structures into a water sphere and propagating for 2.5 ps utilizing classical MD with time steps of 0.5 fs at a constant temperature of 300 K. We applied a QM/MM approach with electrostatic embedding in which the catalyst and the nearest 10 ($[Ru(bda)(pic)_2]$), 13 (**MC1**) and 25 (**MC3**) water molecules were included into the QM model. We have chosen the respective number of quantum-mechanically treated water molecules so that spheres of 5 Å around the binding sites of all ruthenium atoms are filled with water, including the important carboxy ligands. Additional water molecules were added for the bigger macrocycles to fill the cavity between the three centers, and therefore, to ensure the proper description of cooperativity effects. The applied QM/MM interface accounts for non-covalent interactions, whereas proton diffusion to the surrounding solvent is not possible in our model, but also not to be expected on the time scale of our simulations. QM calculations were performed at the PBE/def2-SVP level in Turbomole.[10] The TIP-3P force field [11] was applied to the surrounding classical water utilizing Tinker package [12] and including water molecules with a maximum distance of 2.0 nm (for $[Ru(bda)(pic)_2]$) and 1.2 nm (for **MC1**–**MC3**) to the catalyst. Van der Waals parameters for the QM system were taken from the OPLS-aa force field [13] (organic ligands) and the UFF force field [14] (ruthenium atoms, explicit water), respectively. After 1.0 ps of equilibration, 30 structures were sampled along the trajectory in equal time steps of 50 fs. Vertical excitation energies were then calculated for each structure using the long-range corrected CAM-B3LYP functional [15] with the def2-SVP basis set as implemented in Gaussian09.[16] Ensemble absorption spectra were obtained by convolution of each set of oscillator strengths with Lorentzian functions of 20 nm width.

For the dynamic exploration of reaction pathways, starting structures generated as described above were propagated within the same QM/MM approach. In order to model the oxidation steps, one electron per ruthenium center was removed in every simulated reaction step and the relaxation of the solvated catalyst in the respective oxidation state was observed using MD. Reactive trajectories were propagated with time steps of 0.25 fs at a constant temperature of 500 K in order to speed up the reaction. Oxygen liberation has been observed after removing three electrons from the default $[Ru^{V}=O|Ru^{V}=O|Ru^{V}=O]^{3+}$ species of **MC3** and one electron from the $[Ru^{V}=O]^{+}$ species of $[Ru(bda)(pic)_2]$. The nucleophilic attack of water is accompanied by the release of one proton and the change from singlet to triplet state enables the second proton transfer and liberation of elemental dioxygen. The MD simulations for all oxidation steps and the oxygen liberation of **MC3** have been combined to a video, which is added as additional supplementary material.

2. Macrocycle Synthesis and Characterization

[Ru(bda)(bp)]$_3$ (**MC1**):

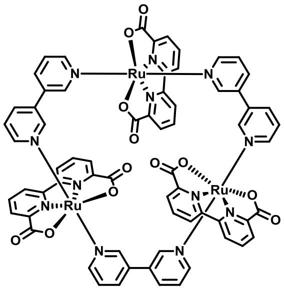

[Ru(bda)(dmso)$_2$] (280 mg, 560 µmol) and 3,3’-bipyridine (79.0 mg, 506 µmol) were dissolved in 150 mL of a degassed 5:1 chloroform/methanol mixture and stirred at 60 °C for 23 hours under a nitrogen atmosphere. The solvent was then removed under reduced pressure. The crude was taken up in dichloromethane/methanol and purified over Al_2O_3 (15% w/w H_2O, CH_2Cl_2/MeOH 6:1) several times. The product was obtained as a red-brown solid (65.0 mg, 43.3 µmol, 26%).

^{1}H NMR (400 MHz, CD_2Cl_2/MeOD 5:1, ascorbic acid): δ = 8.85 (brs, 6H), 8.66 (d, J = 7.9 Hz, 6H), 8.14 (d, J = 7.7 Hz, 6H), 7.92 (t, J = 7.9 Hz, 6H), 7.65 (d, J = 7.9 Hz, 6H), 7.16-7.05 (m, 12H) ppm. **^{13}C NMR** (101 MHz, CD_2Cl_2/MeOD 5:1, ascorbic acid): δ = 174.1, 160.2, 157.4, 152.5, 150.4, 136.2, 134.1, 133.0, 127.0, 125.8, 125.7 ppm. **ESI-HRMS** (pos. mode, $CHCl_3$/MeOH 3:1): m/z = $[M]^+$: measured: 1499.0400, calculated: 1499.0217.

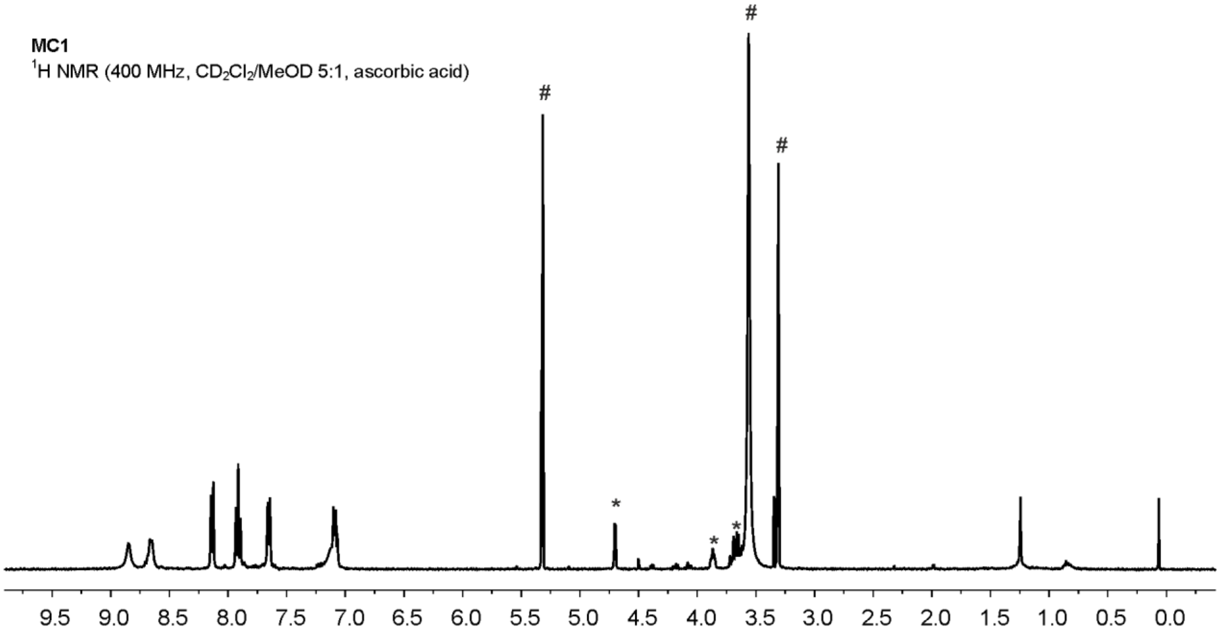

Figure S1. ^{1}H NMR spectrum (400 MHz, CD$_2$Cl$_2$/MeOD 5:1, ascorbic acid) of **MC1**. (# residual solvent, * ascorbic acid)

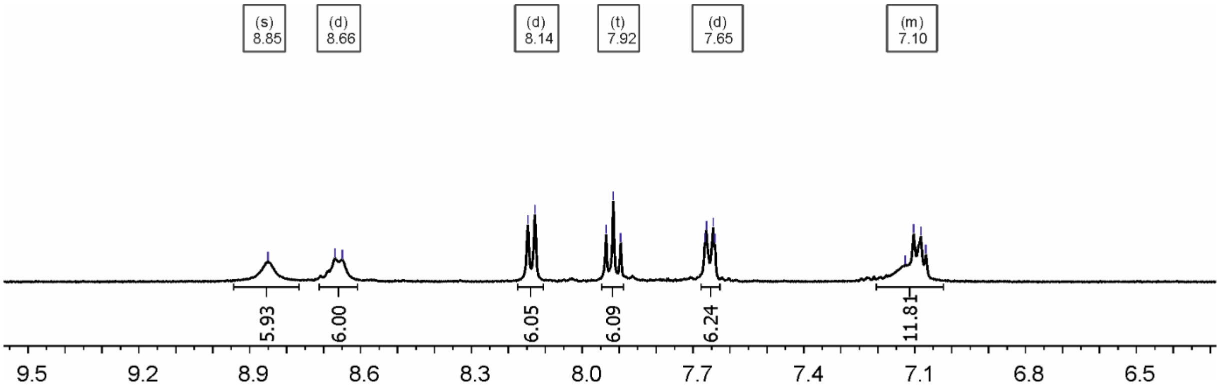

Figure S2. Aromatic region of the ^{1}H NMR spectrum (400 MHz, CD$_2$Cl$_2$/MeOD 5:1, ascorbic acid) of **MC1**.

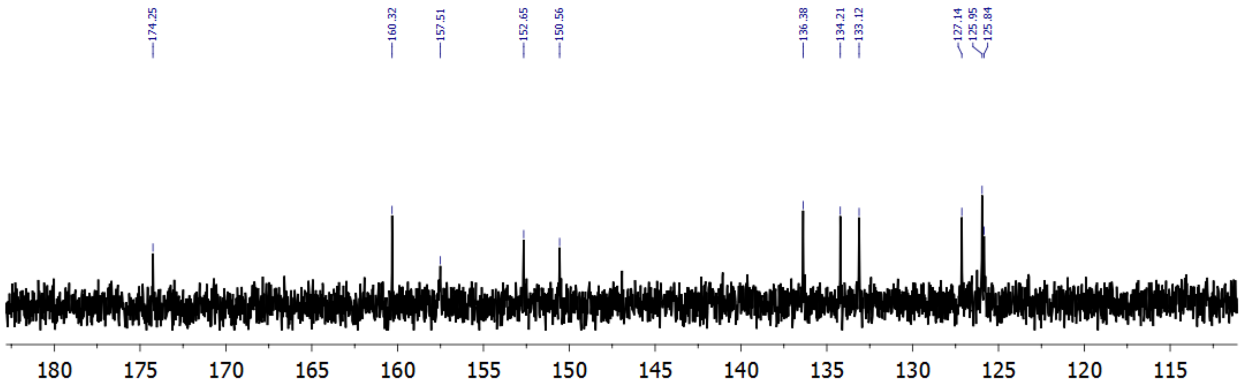

Figure S3. ^{13}C NMR spectrum (101 MHz, CD_2Cl_2/MeOD 5:1, ascorbic acid) of **MC1**.

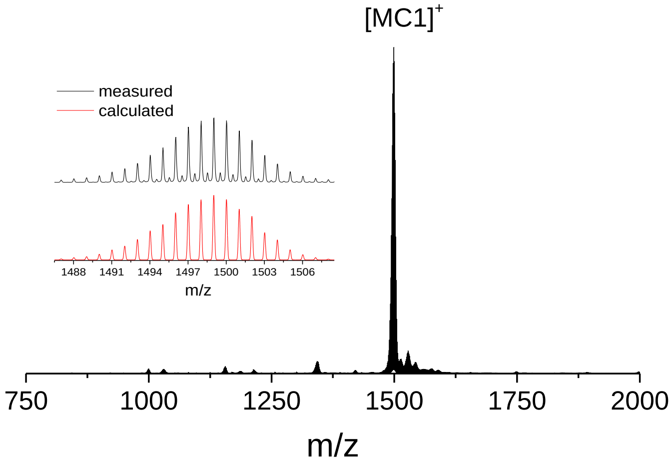

Figure S4. HR-ESI mass spectrum of **MC1** with the inset showing the measured and the calculated isotopic distribution.

$[Ru(bda)(bpe)]_3$ (**MC2**):

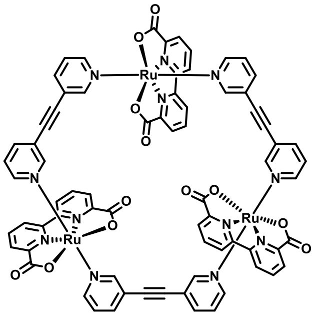

$[Ru(bda)(dmso)_2]$ (554 mg, 1.11 mmol) and 1,2-di(pyridin-3'-yl)-ethyne (200 mg, 1.11 mmol) were dissolved in 150 mL of a degassed 1:1 chloroform/methanol mixture and stirred at 60 °C for 20 hours under a nitrogen atmosphere. After the solvent was removed under reduced pressure the crude was taken up in dichloromethane/methanol and purified over Al_2O_3 (15% w/w H_2O, CH_2Cl_2/MeOH 9:1) several times. After letting the solvent evaporate slowly, the product was obtained as dark crystals. The crystals were filtered off, washed with diethyl ether and dried in high vacuum (90 mg, 57.3 µmol, 16%).

^{1}H NMR (400 MHz, CD_2Cl_2/MeOD 5:1, ascorbic acid) δ = 8.73 (d, J = 7.1 Hz, 6H), 8.33 (s, 6H), 8.12 (dd, J = 7.8, 1.1 Hz, 6H), 7.99 (t, J = 7.9 Hz, 6H), 7.67 – 7.63 (m, 6H), 7.52 (d, J = 5.5 Hz, 6H), 7.07 (dd, J = 7.6, 6.1 Hz, 6H) ppm. **^{13}C NMR** (101 MHz, CD_2Cl_2/MeOD 5:1, ascorbic acid): δ = 174.2, 160.4, 157.6, 156.3, 151.3, 139.8, 133.4, 127.1, 125.8, 125.4, 121.2, 89.2 ppm. **HRMS** (pos. mode, $CHCl_3$/MeOH 3:1): m/z = $[M+Na]^+$: measured: 1594.0150, calculated: 1594.0108.

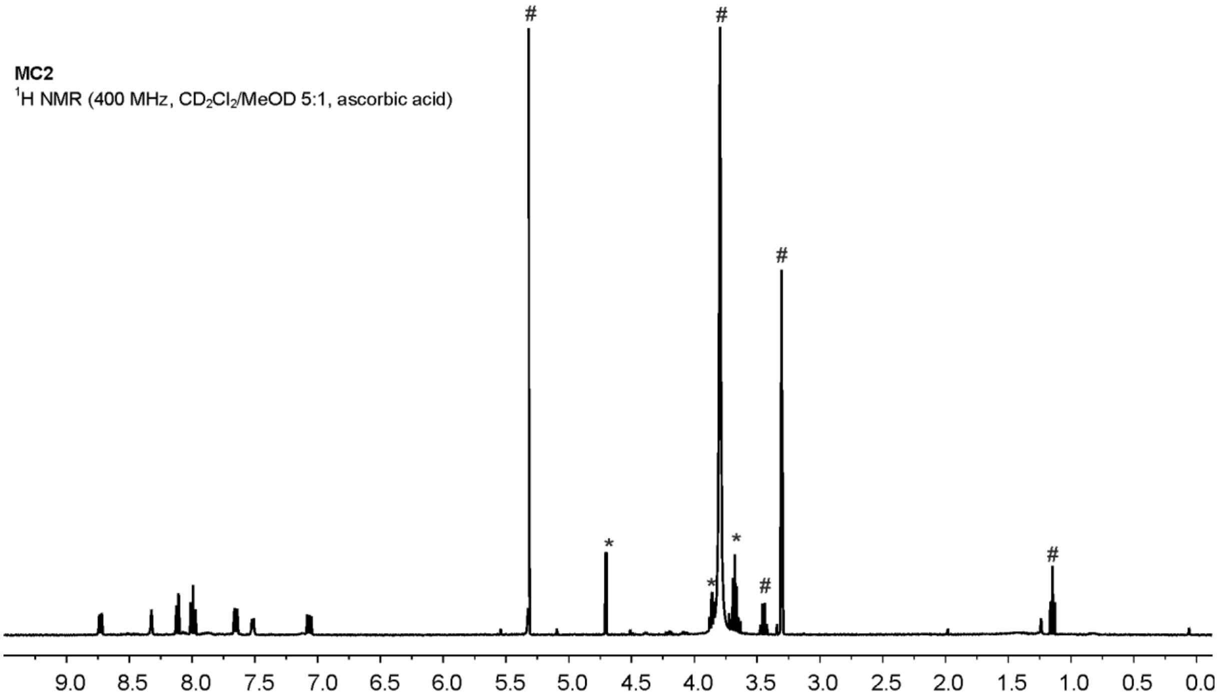

Figure S5. ^{1}H NMR spectrum (400 MHz, CD_2Cl_2/MeOD 5:1, ascorbic acid) of **MC2**. (# residual solvent, * ascorbic acid)

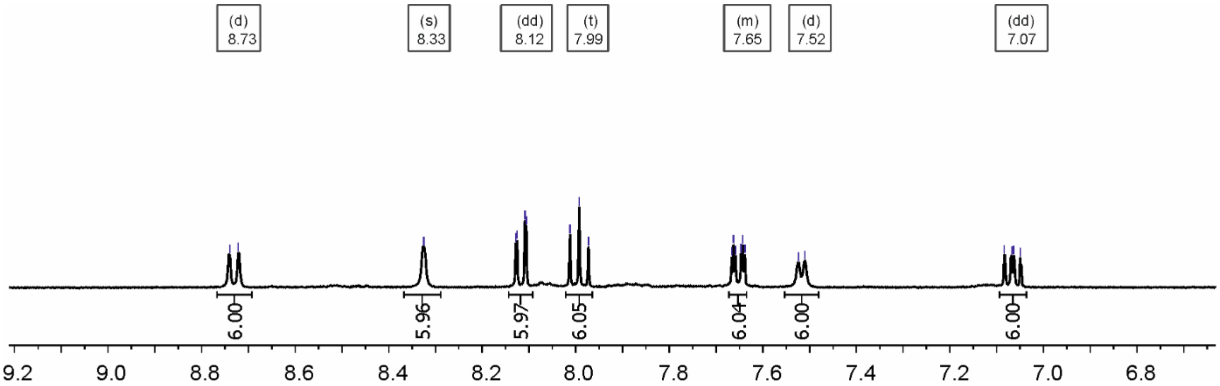

Figure S6. Aromatic region of the ^{1}H NMR spectrum (400 MHz, CD_2Cl_2/MeOD 5:1, ascorbic acid) of **MC2**.

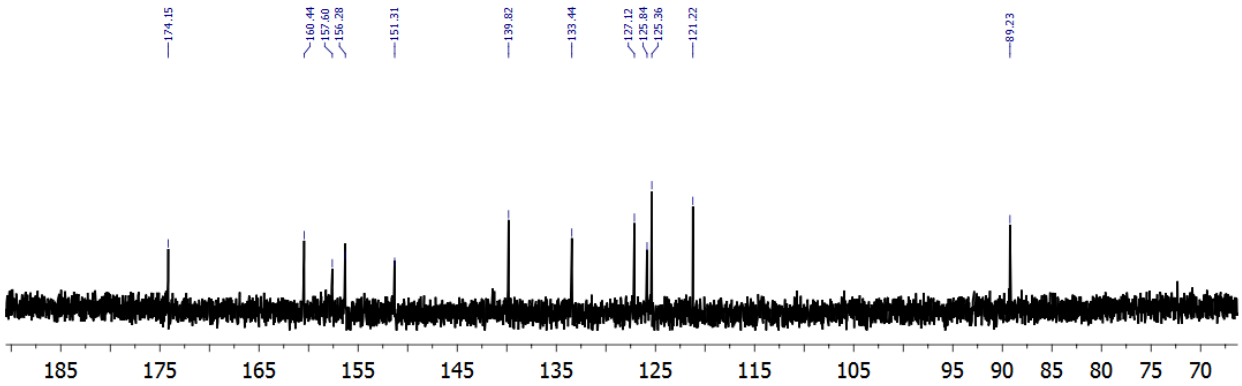

Figure S7. ^{13}C NMR spectrum (101 MHz, CD_2Cl_2/MeOD 5:1, ascorbic acid) of **MC2**.

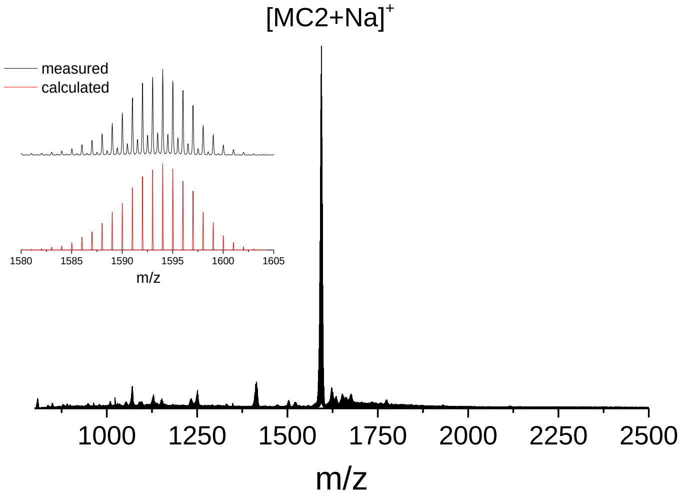

Figure S8. HR-ESI mass spectrum of **MC2** with the inset showing the measured and the calculated isotopic distribution.

[Ru(bda)(bpbp)]$_3$ (**MC4**):

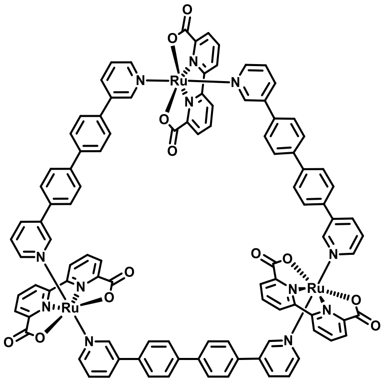

[Ru(bda)(dmso)$_2$] (303 mg, 607 µmol) and 4,4'-bis(pyridin-3''-yl)-1,1'-biphenyl (178 mg, 579 µmol) were dissolved in 200 mL of a degassed 5:1 chloroform/methanol mixture and stirred at 60 °C for 14 hours under a nitrogen atmosphere. The solvent was removed under reduced pressure and purification over Al_2O_3 (15% w/w H_2O, CH_2Cl_2/MeOH 5:1) and subsequent crystallization from the same solution afforded the product as of dark brown crystals (128 mg, 65.5 µmol, 34%).

^{1}H NMR (400 MHz, CD_2Cl_2/MeOD/CF_3CH_2OH 5:1:0.2, ascorbic acid): δ = 8.50 (d, J = 2.0 Hz, 6H), 8.47 (dd, J = 8.2, 1.0 Hz, 6H), 8.11 (dd, J = 7.8, 1.0 Hz, 6H), 7.90 (t, J = 8.1 Hz, 6H), 7.9–7.82 (m, 6H), 7.78 (d, J = 8.5 Hz, 12H), 7.56 (d, J = 8.5 Hz, 12H), 7.38 (dd, J = 5.8, 0.7 Hz, 6H), 7.15 (dd, J = 8.1, 5.7 Hz, 6H) ppm. **^{13}C NMR** (101 MHz, CD_2Cl_2/MeOD/CF_3CH_2OH 5:1:0.2, ascorbic acid): δ = 173.9, 159.8, 156.7, 151.0, 149.2, 140.6, 137.8, 135.0, 134.9, 132.0, 127.7, 127.4, 126.3, 124.9, 124.6 ppm. **HR-MS** (pos. mode, $CHCl_3$/MeOH 1:1): m/z = $[M]^+$: measured: 1955.2116, calculated: 1955.2107.

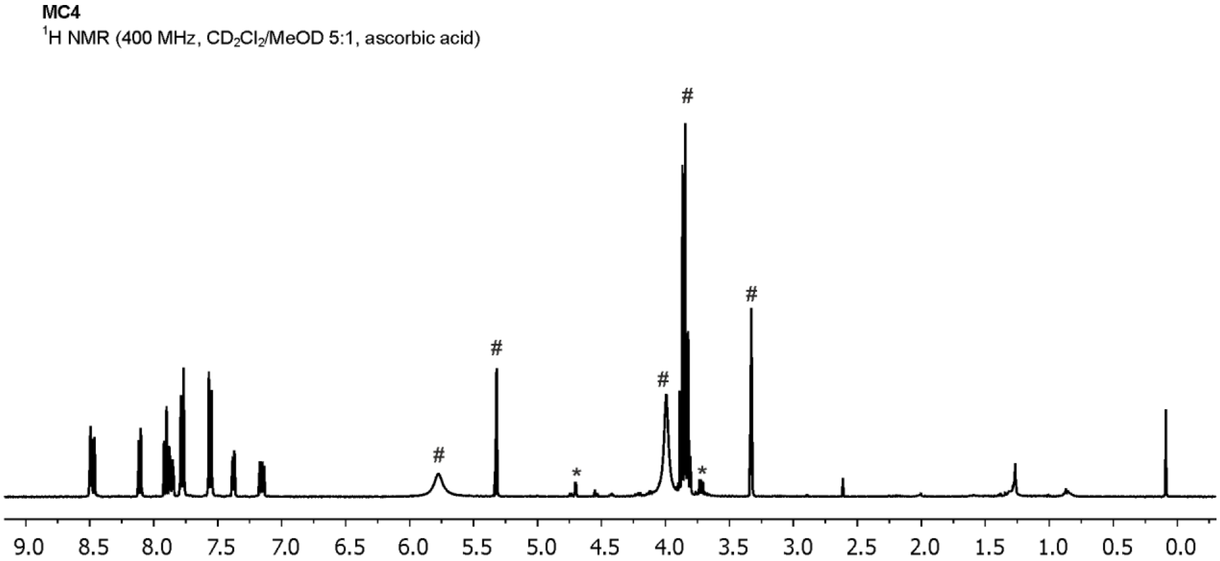

Figure S9. ^{1}H NMR spectrum (400 MHz, CD_2Cl_2/MeOD/CF_3CH_2OH 5:1:0.2, ascorbic acid) of **MC4**. (# residual solvent, * ascorbic acid)

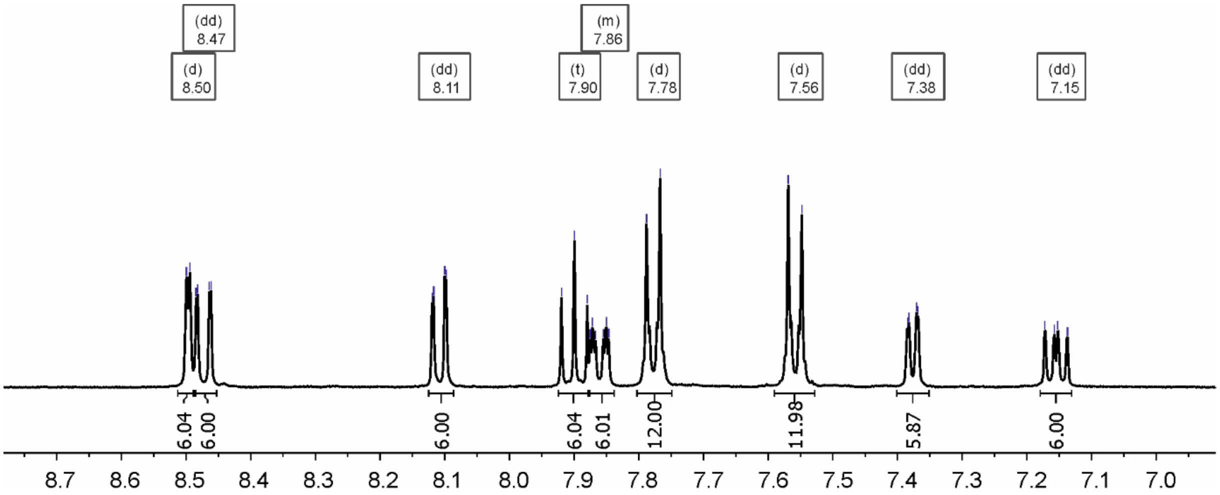

Figure S10. Aromatic region of the ^{1}H NMR spectrum (400 MHz, CD_2Cl_2/MeOD/CF_3CH_2OH 5:1:0.2, ascorbic acid) of **MC4**.

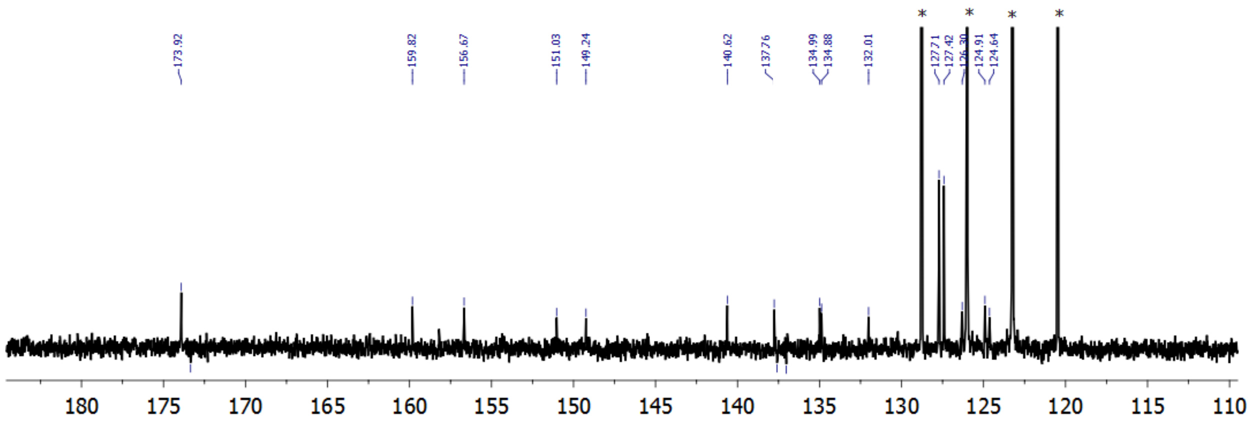

Figure S11. ^{13}C NMR spectrum (101 MHz, CD_2Cl_2/MeOD/CF_3CH_2OH 5:1:0.2, ascorbic acid) of **MC4**. (* CF_3CH_2OH)

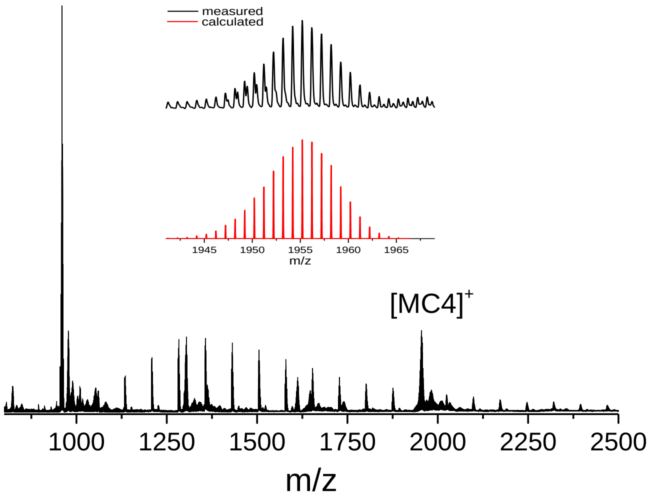

Figure S12. HR-ESI mass spectrum of **MC4** with the inset showing the measured and the calculated isotopic distribution.

3. X-ray Crystallographic Data

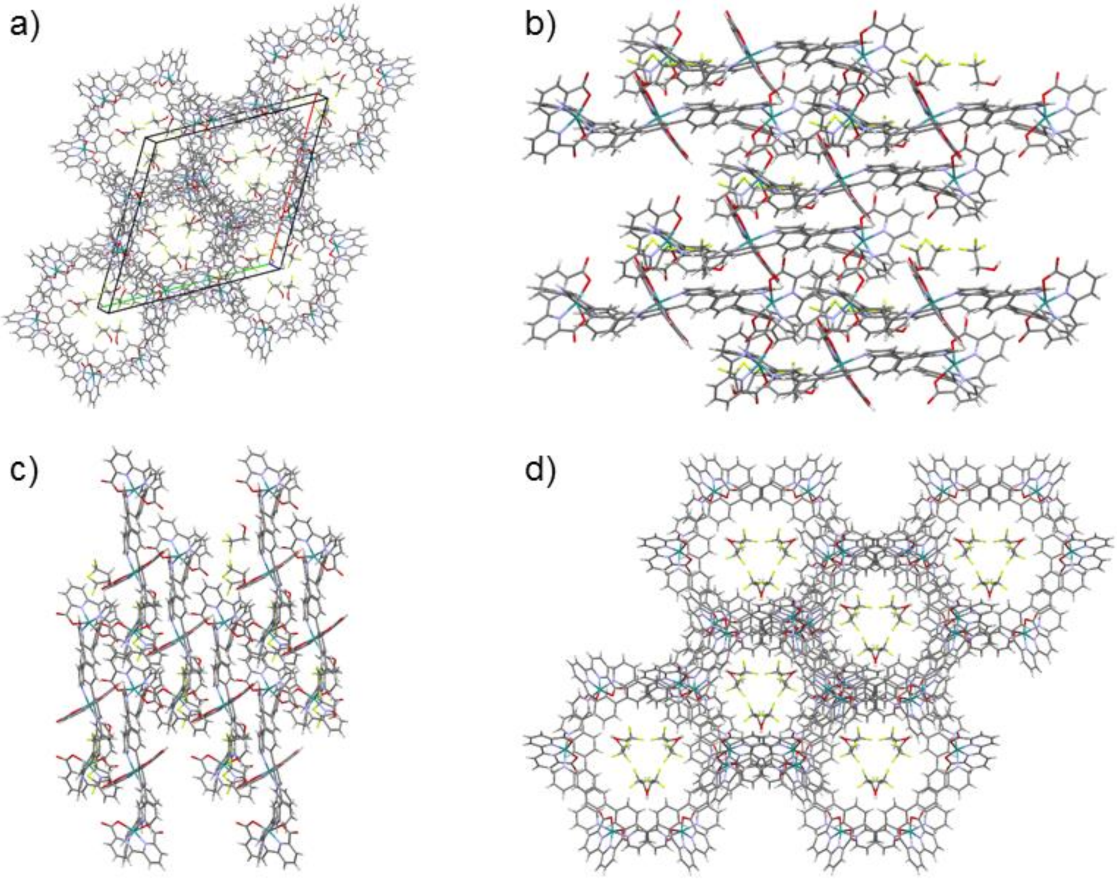

Figure S13. Crystal packing of **MC4** with the unit cell (a) and views along the cell axes a (b), b (c) and c (d). (grey = carbon, white = hydrogen, red = oxygen, purple = nitrogen, turquoise = ruthenium, green = fluorine)

Crystal data for **MC4** ($C_{102}H_{66}N_{12}O_{12}Ru_3$ • 2.47 $C_2H_3F_3O$): Mr = 2201.98, 0.09x0.0.07x0.06 mm^3, trigonal space group R3c, a = 26.1798(15) Å, α = 90°, b = 26.1798(15) Å, β = 90° c = 30.736(3) Å, γ = 120°, V = 18244(3) Å^3, Z = 6, ρ(*calcd)* = 1.203 g·cm^{-3}, μ = 0.437 mm^{-1}, $F_{(000)}$ = 6681, $GooF(F^2)$ = 1.048, R_1 = 0.0407, wR^2 = 0.1020 for I>2σ(I), R_1 = 0.0446, wR^2 = 0.1041 for all data, 8074 unique reflections [θ ≤ 26.136°] with a completeness of 100.0 % and 425 parameters, 32 restraints.

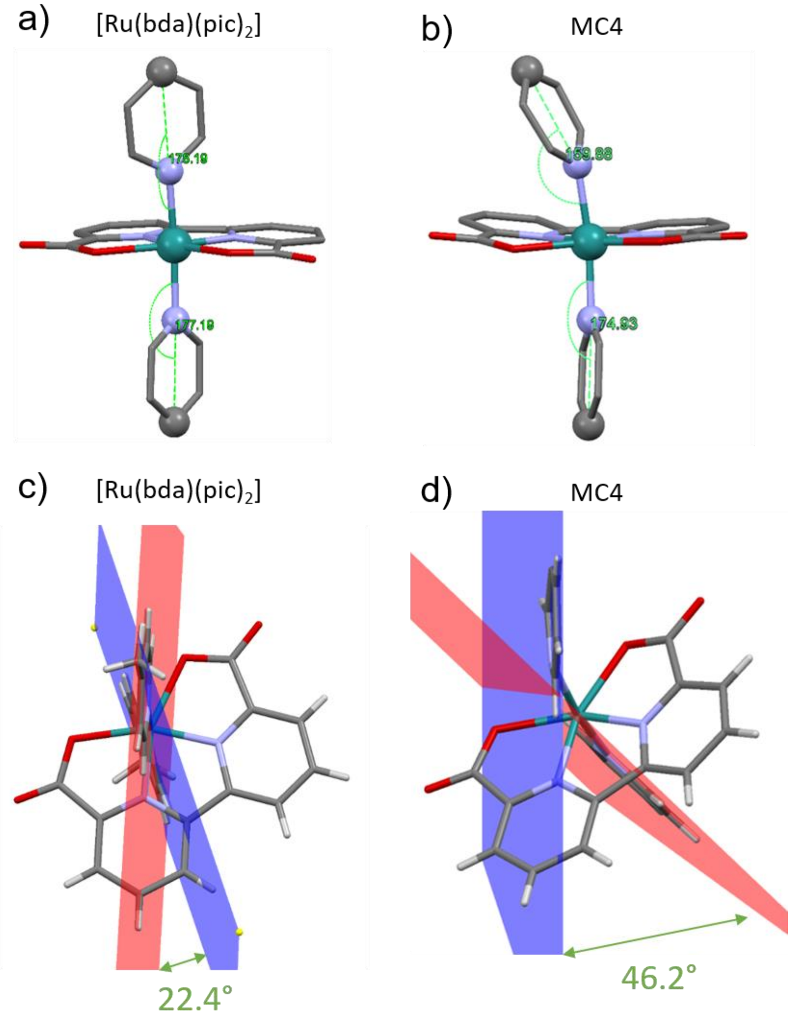

Figure S14. Comparison of the X-ray crystal structures of [Ru(bda)(pic)$_2$] and **MC4** regarding the tilt angle of the axial ligands (a and b) and the torsion angle between the axial ligands (c and d). For **MC4** (b and d) only one Ru(bda) center is displayed, and from the axial ligand only the coordinating pyridine moiety is shown for the sake of clarity. (grey = carbon, white = hydrogen, red = oxygen, purple = nitrogen, turquoise = ruthenium)

4. Calculated Structures

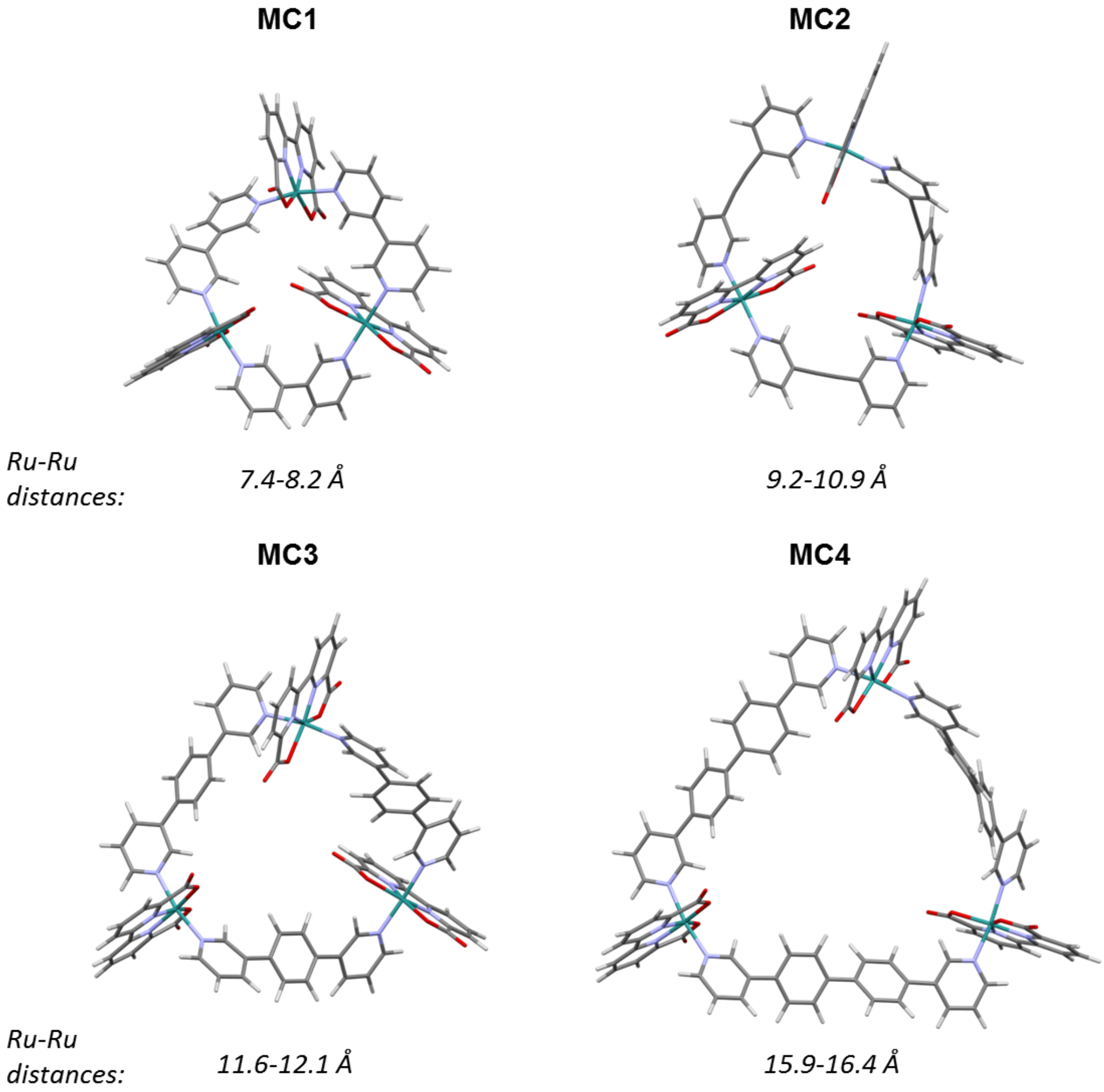

Figure S15. Structures of **MC1**–**MC4** calculated in the [Ru^{II}|Ru^{II}|Ru^{II}] state using DFT with the PBE0 functional and the def2-SVP basis set. (grey = carbon, white = hydrogen, red = oxygen, purple = nitrogen, turquoise = ruthenium)

5. **Electrochemistry**

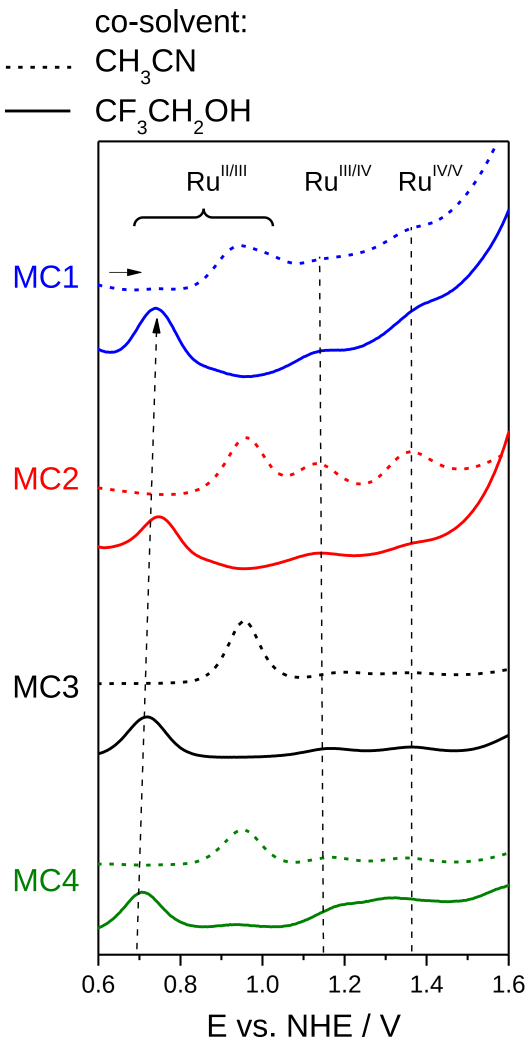

Figure S16. Differential pulse voltamograms (DPVs) for all macrocycles with two different co-solvents (solid lines = 2,2,2-trifluoroethanol, dotted lines = acetonitrile) in a 1:1 mixture with water (pH 1, acid: CF_3SO_3H).

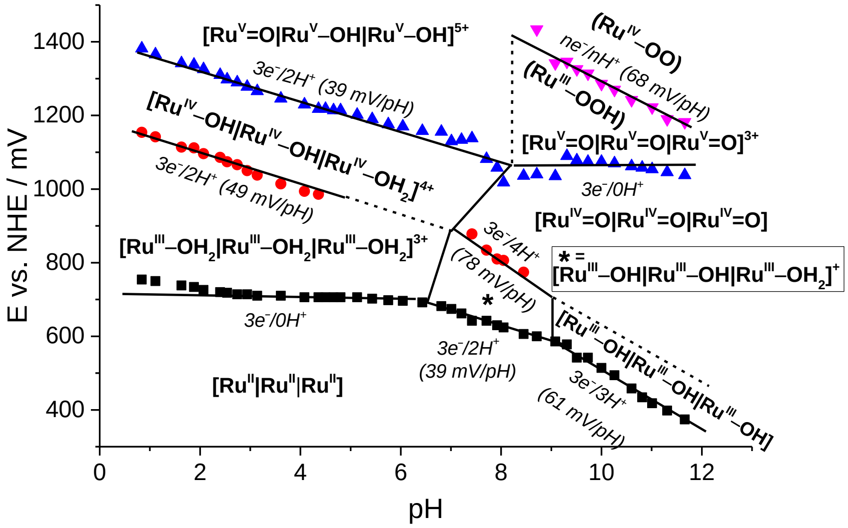

Figure S17. Pourbaix diagram of **MC1**. The potentials were obtained from differential pulse voltammetry at certain pH values which were adjusted by stepwise addition of NaOH solutions to a 1:1 CF_3CH_2OH/H_2O (pH 1, acid: CF_3SO_3H) solution.

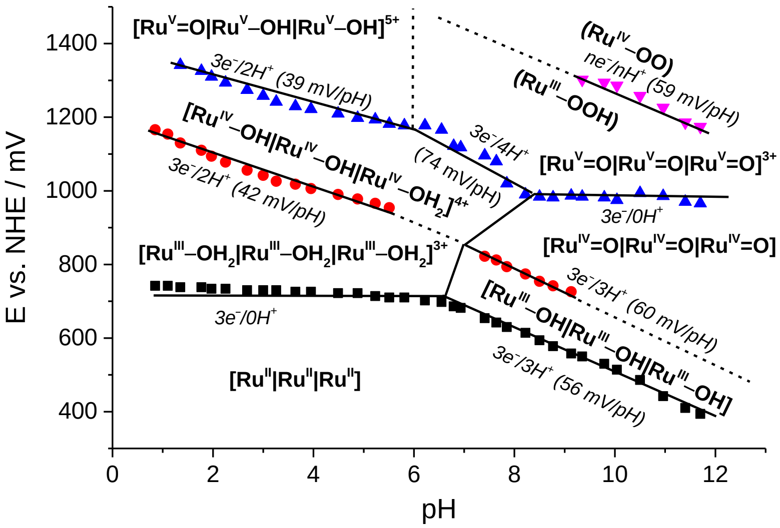

Figure S18. Pourbaix diagram of **MC2**. The potentials were obtained from differential pulse voltammetry at certain pH values which were adjusted by stepwise addition of NaOH solutions to a 1:1 CF_3CH_2OH/H_2O (pH 1, acid: CF_3SO_3H) solution.

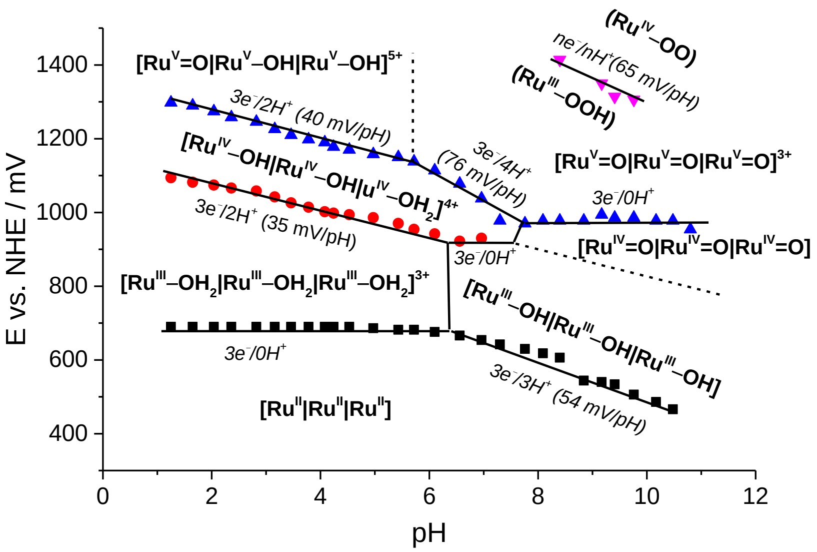

Figure S19. Pourbaix diagram of **MC3**. The potentials were obtained from differential pulse voltammetry at certain pH values which were adjusted by stepwise addition of NaOH solutions to a 1:1 CF_3CH_2OH/H_2O (pH 1, acid: CF_3SO_3H) solution.

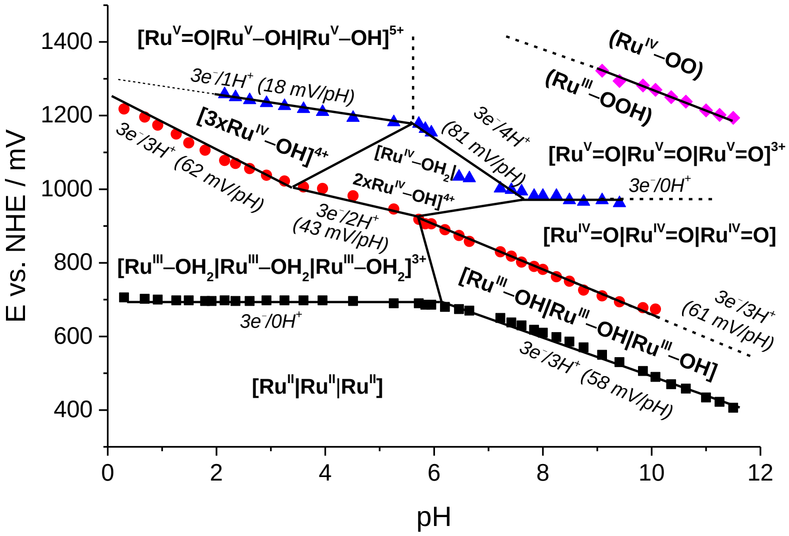

Figure S20. Pourbaix diagram of **MC4**. The potentials were obtained from differential pulse voltammetry at certain pH values which were adjusted by stepwise addition of NaOH solutions to a 1:1 CF_3CH_2OH/H_2O (pH 1, acid: CF_3SO_3H) solution.

6. UV/Vis Spectroscopy

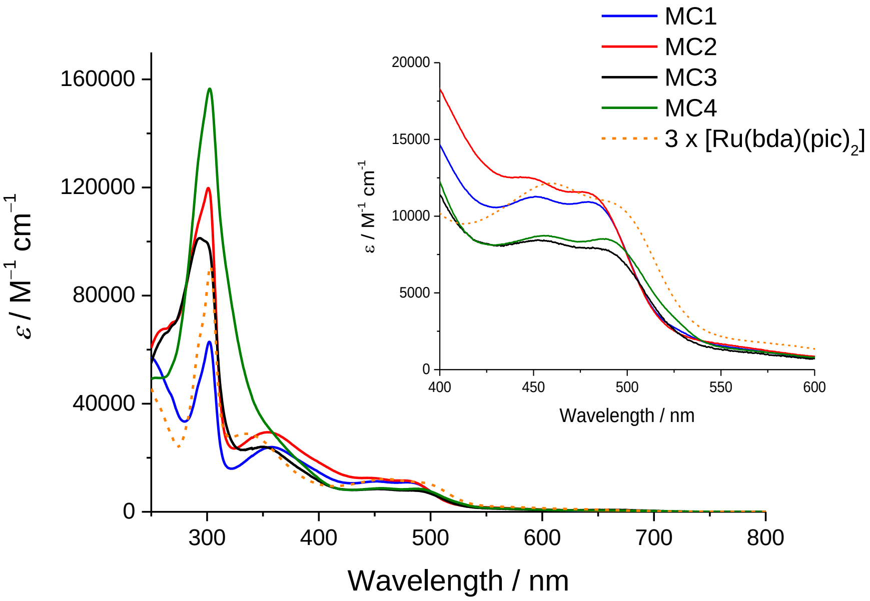

Figure S21. UV/Vis spectra of all macrocycles **MC1**–**MC4** and the mononuclear reference complex [Ru(bda)(pic)$_2$] in the Ru(II) oxidation state measured in CH_3CN/H_2O (pH 1, acid: CF_3SO_3H) 1:1 at a concentration of 10^{-5} M.

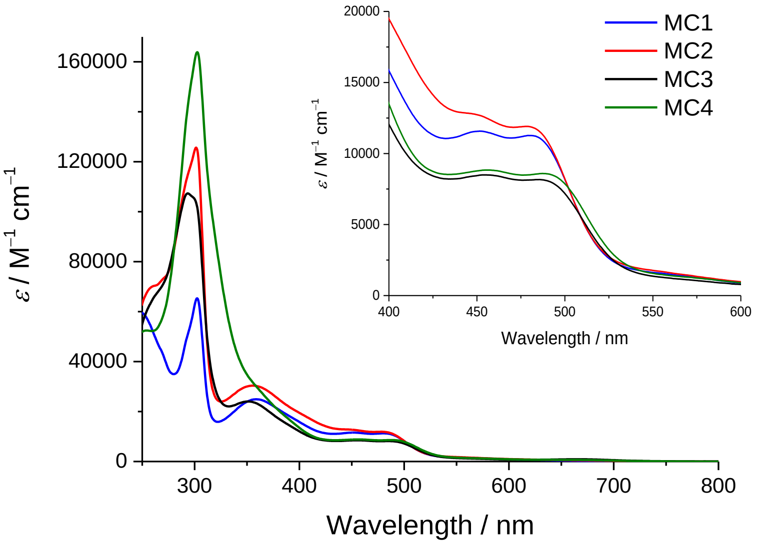

Figure S22. UV/Vis spectra of all macrocycles **MC1**–**MC4** in the Ru(II) oxidation state measured in CH_3CN/H_2O (pH 1, acid: CF_3SO_3H) 4:1 at a concentration of 10^{-5} M.

7. Spectroelectrochemistry

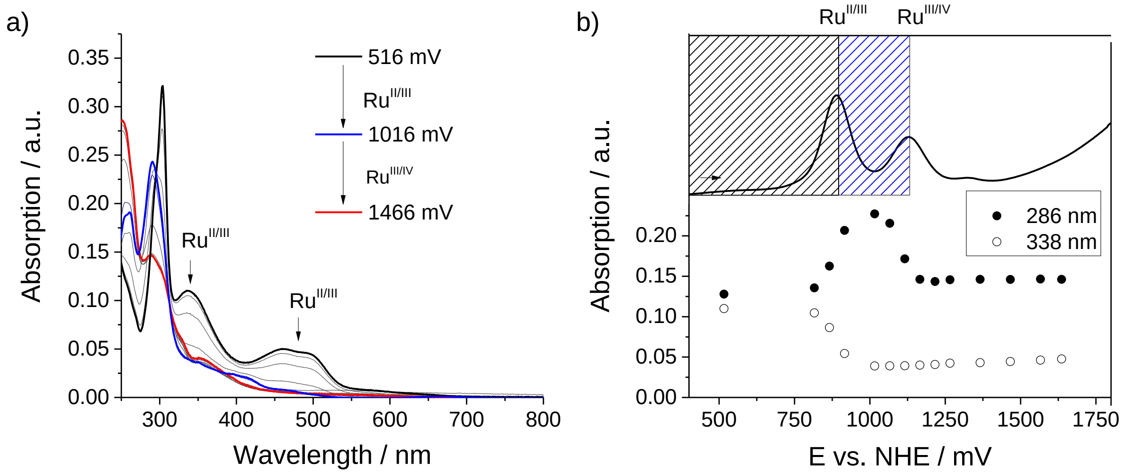

Figure S23. (a) Spectroelectrochemistry for [Ru(bda)(pic)$_2$] in 1:1 CH_3CN/H_2O (pH 1, acid: CF_3SO_3H). (b) DPV in the same solvent mixture and monitoring of different absorption wavelength over the applied potential derived from the spectroelectrochemistry.

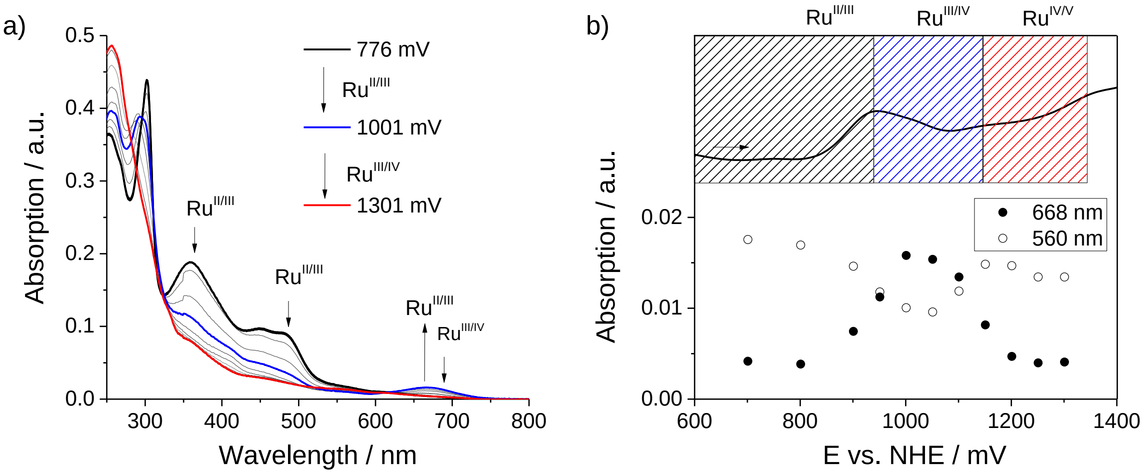

Figure S24. (a) Spectroelectrochemistry for **MC1** in 1:1 CH_3CN/H_2O (pH 1, acid: CF_3SO_3H). (b) DPV in the same solvent mixture and monitoring of different absorption wavelength over the applied potential derived from the spectroelectrochemistry.

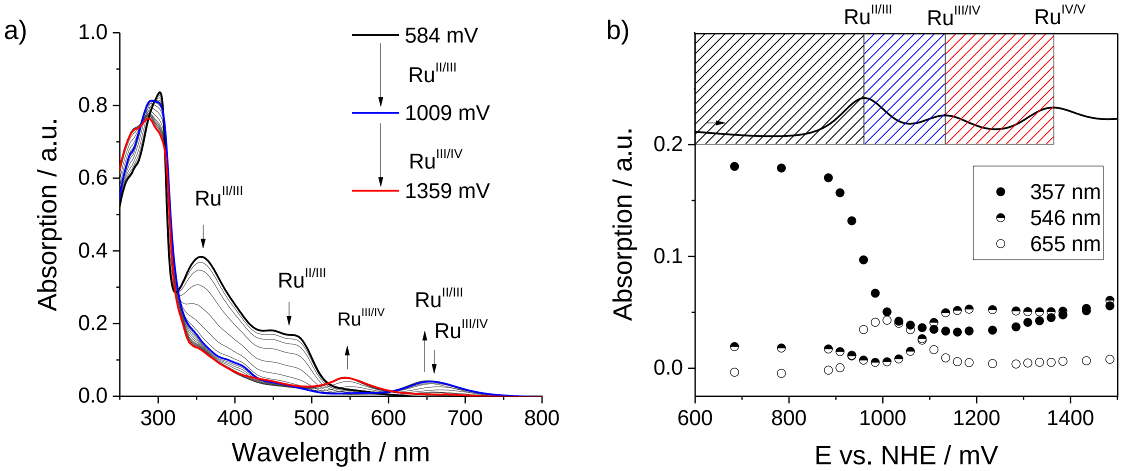

Figure S25. (a) Spectroelectrochemistry for **MC2** in 1:1 CH_3CN/H_2O (pH 1, acid: CF_3SO_3H). (b) DPV in the same solvent mixture and monitoring of different absorption wavelength over the applied potential derived from the spectroelectrochemistry.

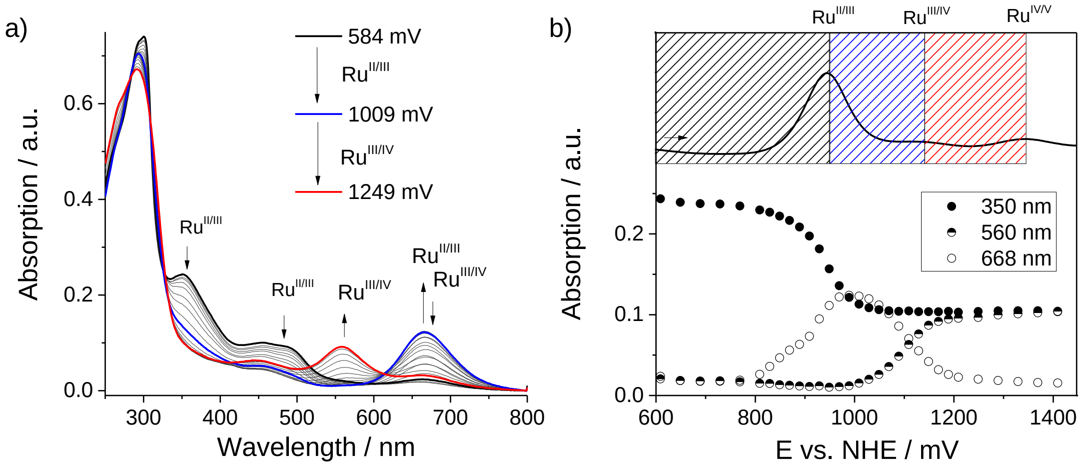

Figure S26. (a) Spectroelectrochemistry for **MC3** in 1:1 CH_3CN/H_2O (pH 1, acid: CF_3SO_3H). (b) DPV in the same solvent mixture and monitoring of different absorption wavelength over the applied potential derived from the spectroelectrochemistry.

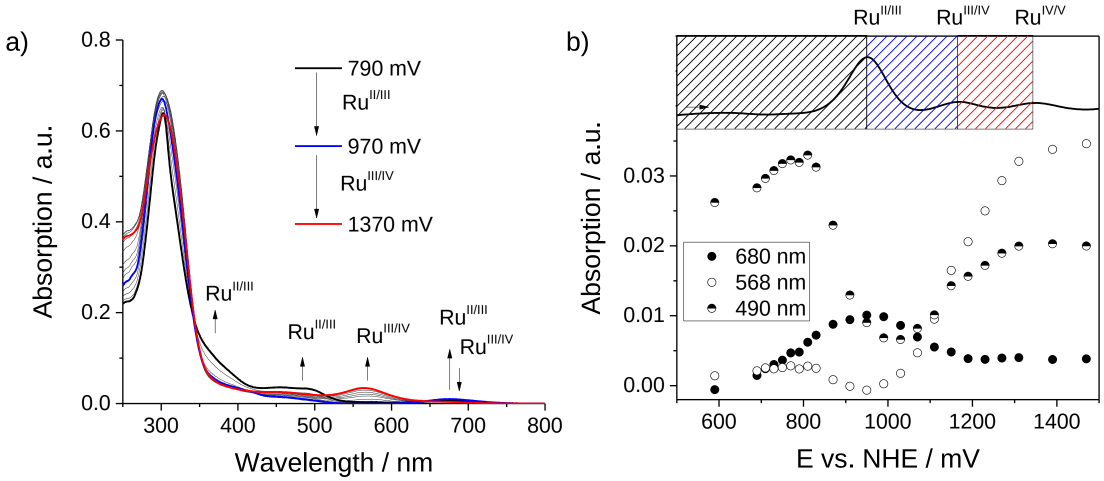

Figure S27. (a) Spectroelectrochemistry for **MC4** in 4:1 CH_3CN/H_2O (pH 1, acid: CF_3SO_3H). (b) DPV in the same solvent mixture and monitoring of different absorption wavelength over the applied potential derived from the spectroelectrochemistry.

8. Spectra Simulation

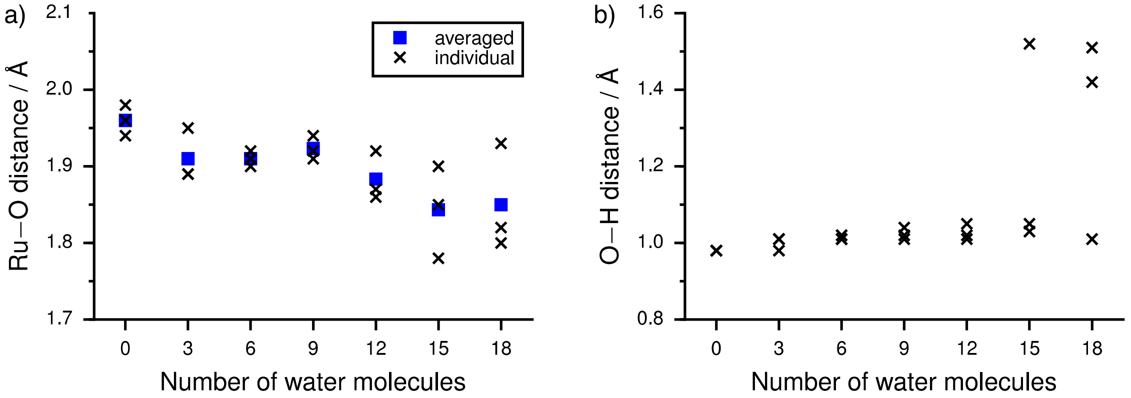

Figure S28. Influence of the amount of explicit water molecules on important properties of **MC3** in the Ru^{IV} state. (a) Ru–OH distance against the number of water molecules for each individual center and averaged. (b) RuO–H distance against the number of water molecules.

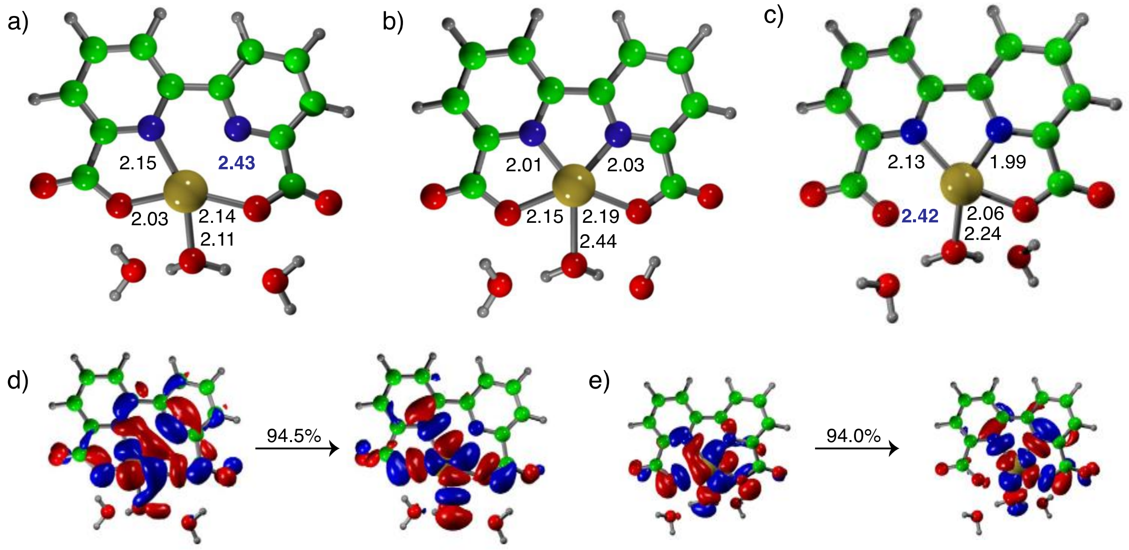

Figure S29. Comparison of different structural motifs in the Ru^{III} state of [Ru(bda)(pic)$_2$]. Twisted, flat and open structures of the bda-ligand are given in (a), (b) and (c) with their respective Ru–O and Ru–N bond distances in Å. Elongated bond lengths are highlighted in blue. Below, the hole and particle NTOs for the $\sigma \rightarrow \sigma^*$ transition are given for the (d) twisted and (e) open bda structure. Only the relevant parts of the molecules are displayed for clarity. (green = carbon, grey = hydrogen, red = oxygen, blue = nitrogen, yellow = ruthenium)

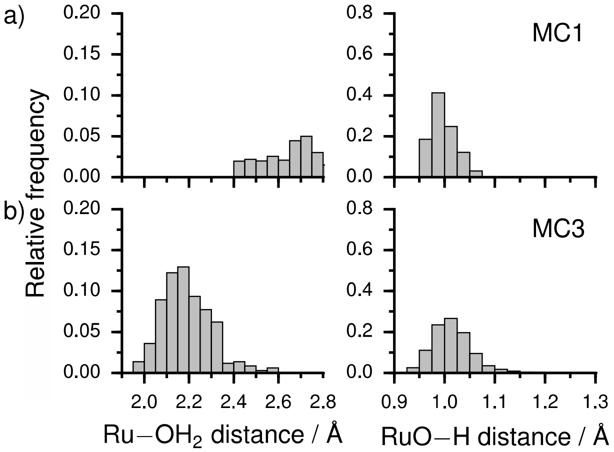

Figure S30. Normalized distributions of the Ru–OH_2 and RuO–H bond lengths for coordinated water molecules in the Ru^{III} state for the compounds **MC1** (a) and **MC3** (b) determined for 30 structures sampled along the molecular dynamics trajectory. Note that for [Ru(bda)(pic)$_2$] no water molecule was found in a distance < 2.8 Å to the ruthenium in all of the 30 structures.

9. Catalysis – Comparable Conditions

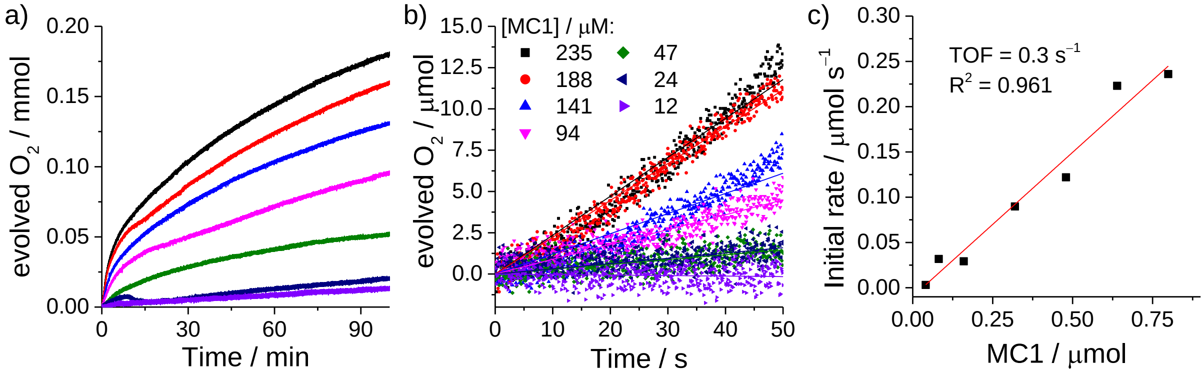

Figure S31. Concentration-dependent oxygen evolution over time for **MC1** as catalyst with 80% (v/v) acetonitrile as a co-solvent at 20 °C(a). Linear regressions through the first 50 s (b) and the plot of the initial rates vs. the catalyst concentration (c). (1.0 g CAN was dissolved in 3.0 mL CH_3CN/H_2O (pH 1, acid: CF_3SO_3H) 4:1 and 400 µL of catalyst solution in CH_3CN/H_2O (pH 1) 4:1 have been injected).

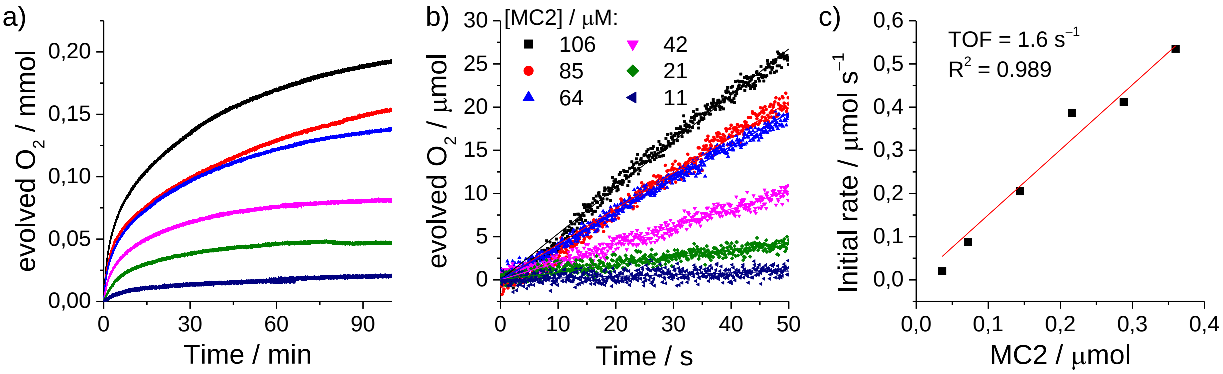

Figure S32. Concentration-dependent oxygen evolution over time for **MC2** as catalyst with 80% (v/v) acetonitrile as a co-solvent at 20 °C (a). Linear regressions through the first 50 s (b) and the plot of the initial rates vs. the catalyst concentration (c). (1.0 g CAN was dissolved in 3.0 mL CH_3CN/H_2O (pH 1, acid: CF_3SO_3H) 4:1 and 400 µL of catalyst solution in CH_3CN/H_2O (pH 1) 4:1 have been injected).

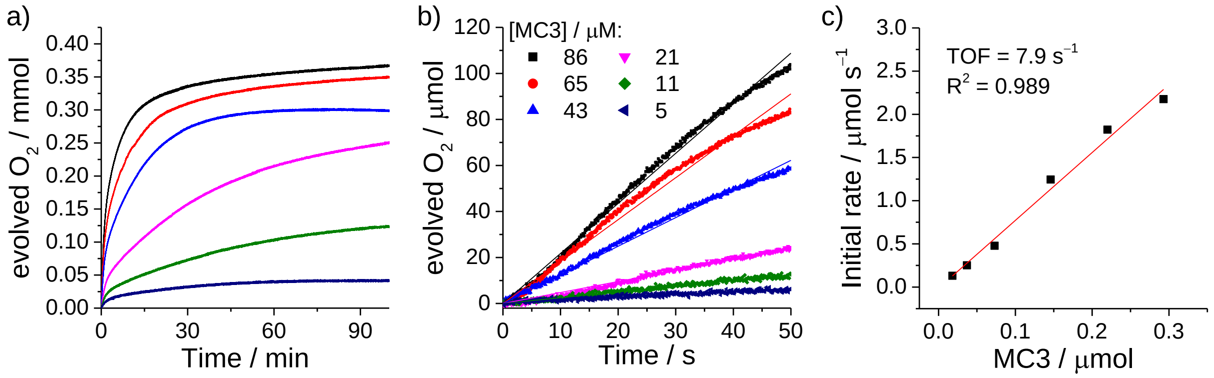

Figure S33. Concentration-dependent oxygen evolution over time for **MC3** as catalyst with 80% (v/v) acetonitrile as a co-solvent at 20 °C (a). Linear regressions through the first 50 s (b) and the plot of the initial rates vs. the catalyst concentration (c). (1.0 g CAN was dissolved in 3.0 mL CH_3CN/H_2O (pH 1, acid: CF_3SO_3H) 4:1 and 400 µL of catalyst solution in CH_3CN/H_2O (pH 1) 4:1 have been injected).

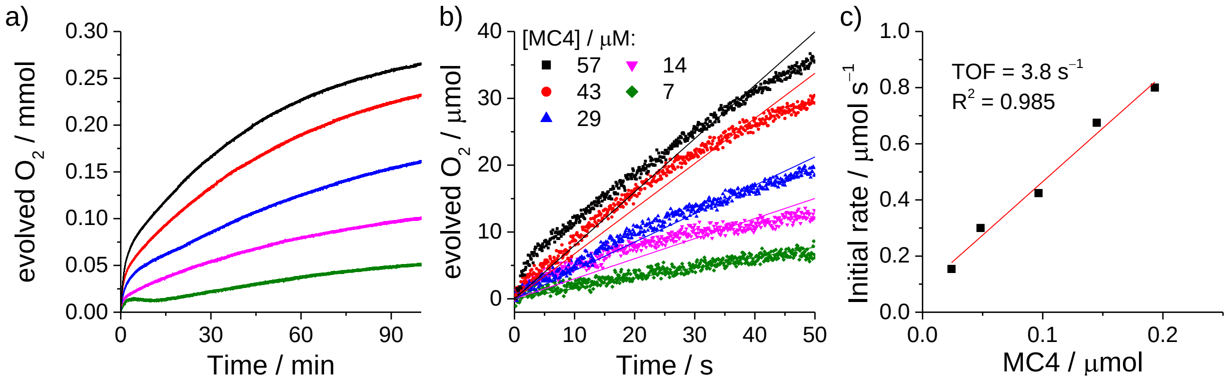

Figure S34. Concentration-dependent oxygen evolution over time for **MC4** as catalyst with 80% (v/v) acetonitrile as a co-solvent at 20 °C (a). Linear regressions through the first 50 s (b) and the plot of the initial rates vs. the catalyst concentration (c). (1.0 g CAN was dissolved in 3.0 mL CH_3CN/H_2O (pH 1, acid: CF_3SO_3H) 4:1 and 400 µL of catalyst solution in CH_3CN/H_2O (pH 1) 4:1 have been injected).

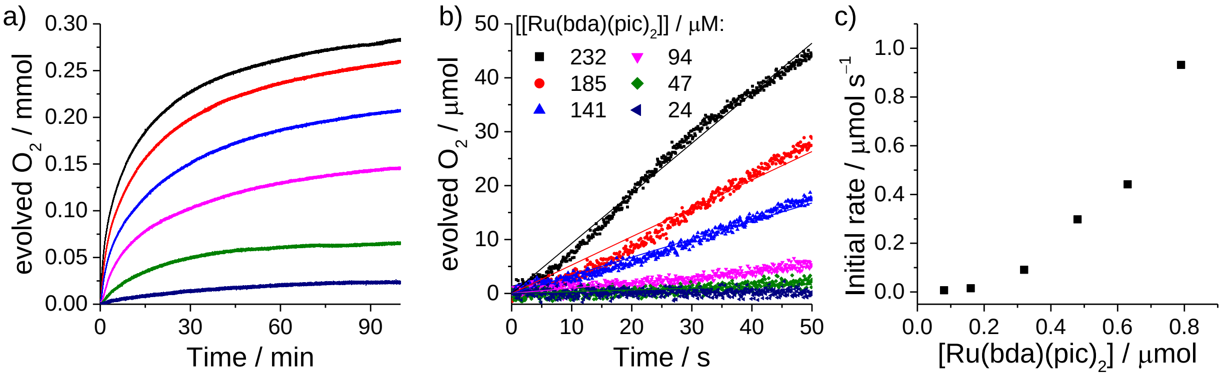

Figure S35. Concentration-dependent oxygen evolution over time for [Ru(bda)(pic)$_2$] as catalyst with 80% (v/v) acetonitrile as a co-solvent at 20 °C (a). Linear regressions through the first linear part (b) and the plot of the initial rates vs. the catalyst concentration (c). (1.0 g CAN was dissolved in 3.0 mL CH_3CN/H_2O (pH 1, acid: CF_3SO_3H) 4:1 and 400 µL of catalyst solution in CH_3CN/H_2O (pH 1) 4:1 have been injected).

10. Catalysis – Optimized Conditions

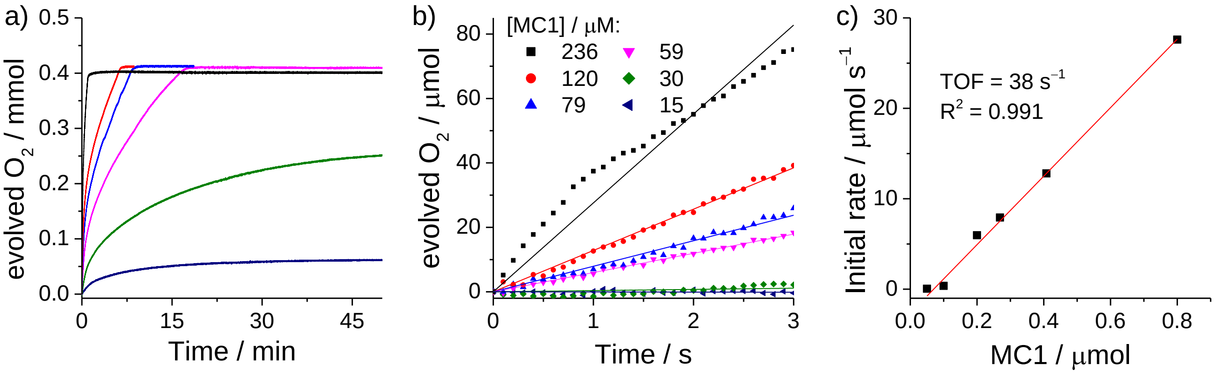

Figure S36. Concentration-dependent oxygen evolution over time for **MC1** as catalyst with 2% (v/v) acetonitrile as co-solvent at 20 °C (a). Linear regressions through the first linear part (b) and the plot of the initial rates vs. the catalyst concentration (c). (1.0 g CAN was dissolved in 3.0 mL H_2O (pH 1, acid: CF_3SO_3H) and 400 µL of catalyst solution in CH_3CN/H_2O (pH 7) 1:9 have been injected).

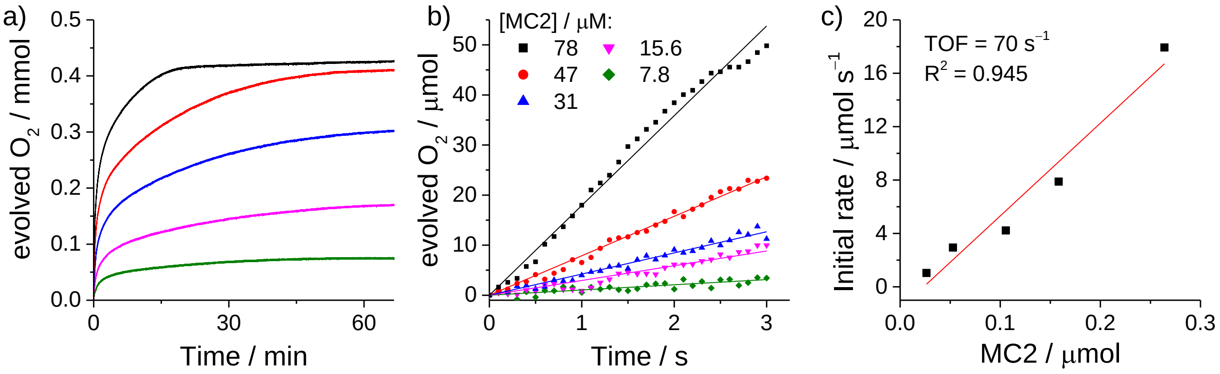

Figure S37. Concentration-dependent oxygen evolution over time for **MC2** as catalyst with 50% (v/v) acetonitrile as a co-solvent at 20 °C (a). Linear regressions through the first linear part (b) and the plot of the initial rates vs. the catalyst concentration (c). (1.0 g CAN was dissolved in 3.0 mL CH_3CN/H_2O (pH 1, acid: CF_3SO_3H) 1:1 and 400 µL of catalyst solution in CH_3CN/H_2O (pH 7) 1:1 have been injected).

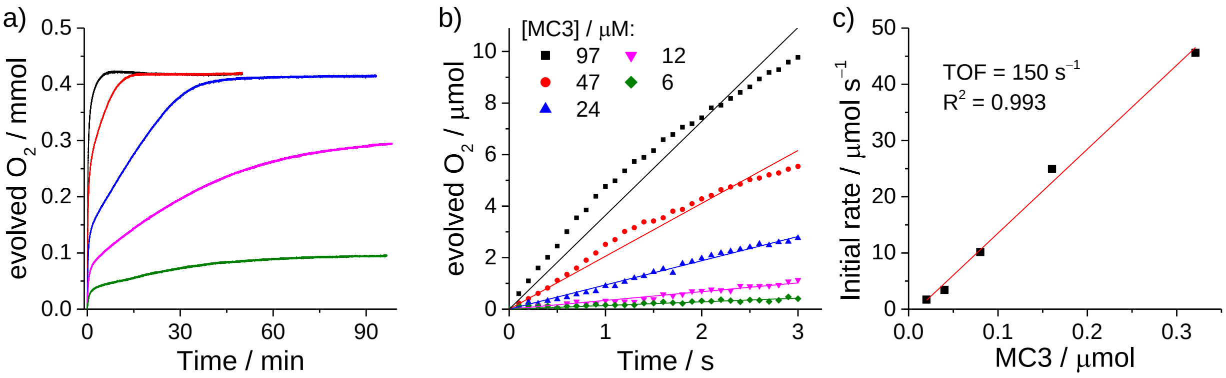

Figure S38. Concentration-dependent oxygen evolution over time for **MC3** as catalyst with 60% acetonitrile as a co-solvent at 20 °C (a). Linear regressions through the first linear part (b) and the plot of the initial rates vs. the catalyst concentration (c). (1.0 g CAN was dissolved in 3.0 mL CH_3CN/H_2O (pH 1, acid: CF_3SO_3H) 3:2 and 400 µL of catalyst solution in CH_3CN/H_2O (pH 7) 3:2 have been injected).

11. Gas Chromatography

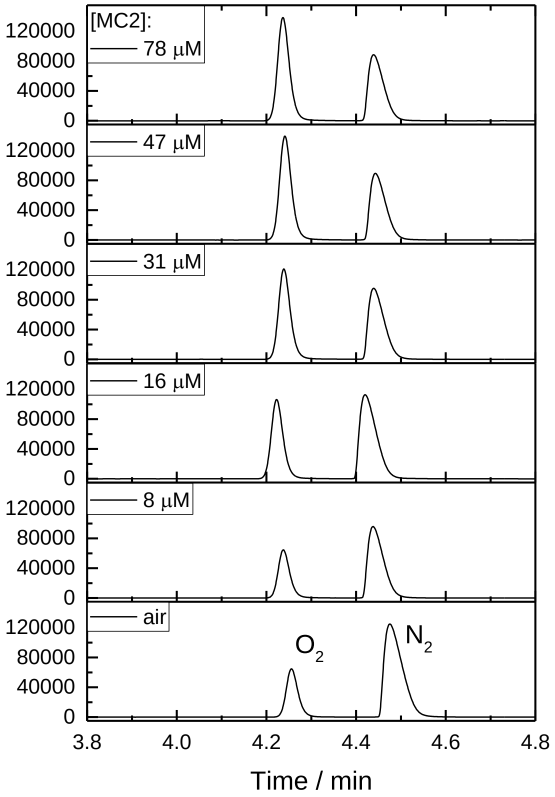

Figure S39. GC chromatograms obtained by the injection of 0.5 mL of the reaction headspace after the completed water oxidation reaction with catalyst **MC2** for different catalyst concentrations and fixed CAN concentration (0.536 M) in 3.4 mL of CH_3CN/H_2O 1:1 (pH 1, acid: CF_3SO_3H). (see Figure S39)

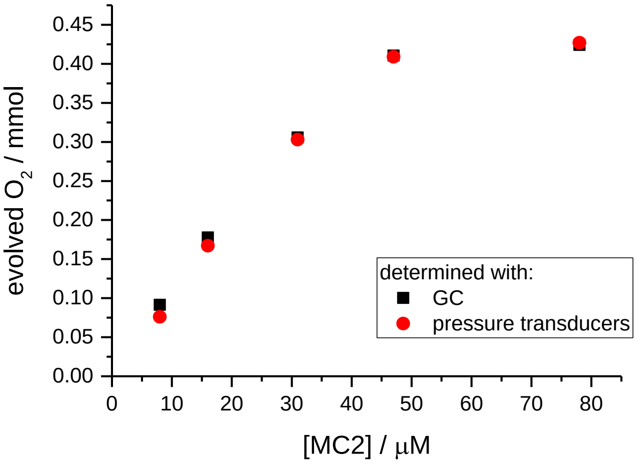

Figure S40: Comparison of the amount of evolved oxygen as determined by GC or by the pressure transducers.

12. CAN consumption – Variation of Catalyst Concentration

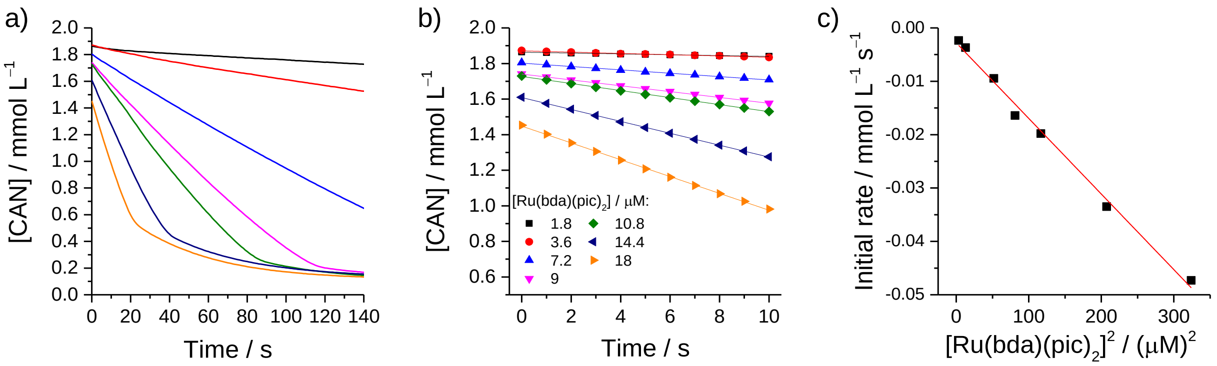

Figure S41. CAN absorbance decay at 360 nm depending on different [Ru(bda)(pic)$_2$] concentrations over 140 s (a), between 0 and 10 s (b), and the plot of the initial rates vs. the catalyst concentration (c). Conditions: [CAN] = 2.0 mM in 2.0 mL 1:1 CH_3CN/H_2O (pH 1) at 25 °C.

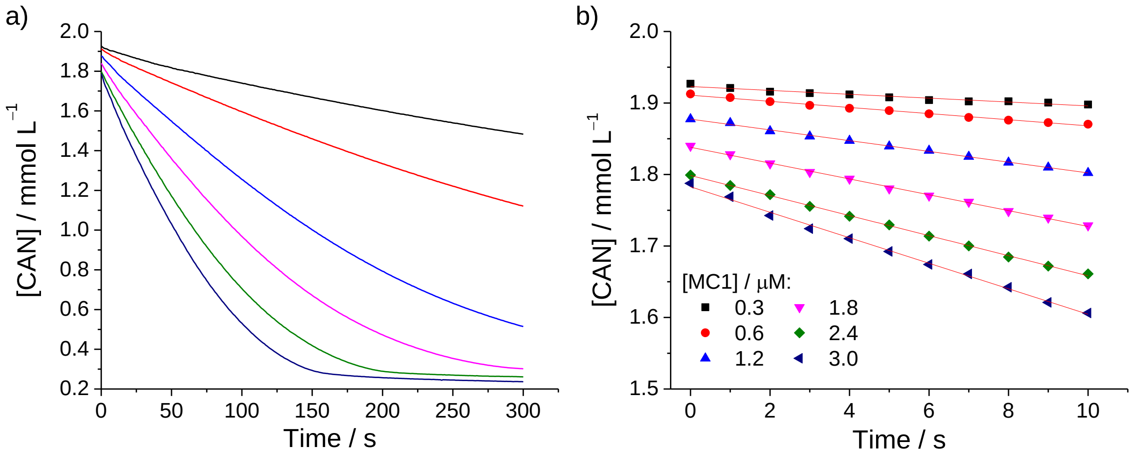

Figure S42. CAN absorbance decay at 360 nm depending on different **MC1** concentrations over 300 s (a), and between 0 and 10 s (b). Conditions: [CAN] = 2.0 mM in 2.0 mL 1:1 CH_3CN/H_2O (pH 1) at 25 °C.

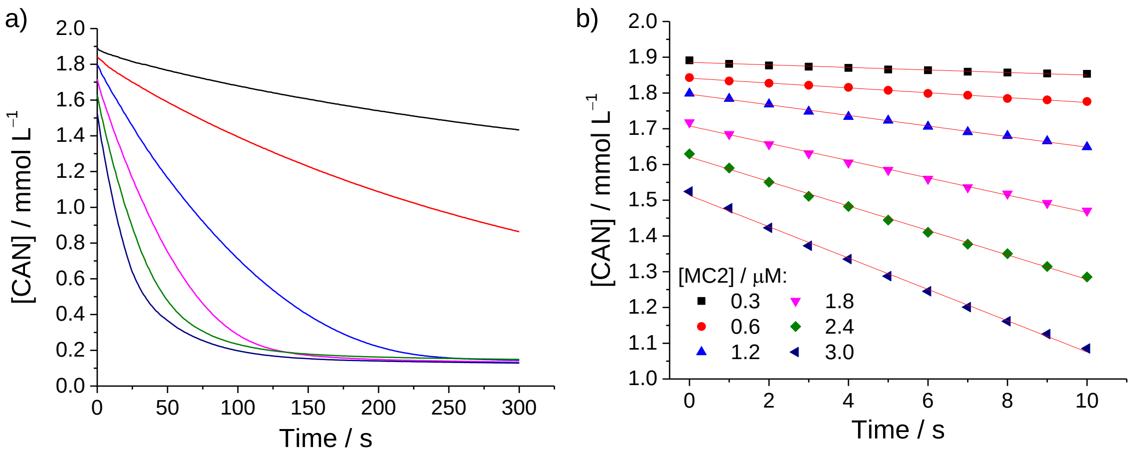

Figure S43. CAN absorbance decay at 360 nm depending on different **MC2** concentrations over 300 s (a), and between 0 and 10 s (b). Conditions: [CAN] = 2.0 mM in 2.0 mL 1:1 CH_3CN/H_2O (pH 1) at 25 °C.

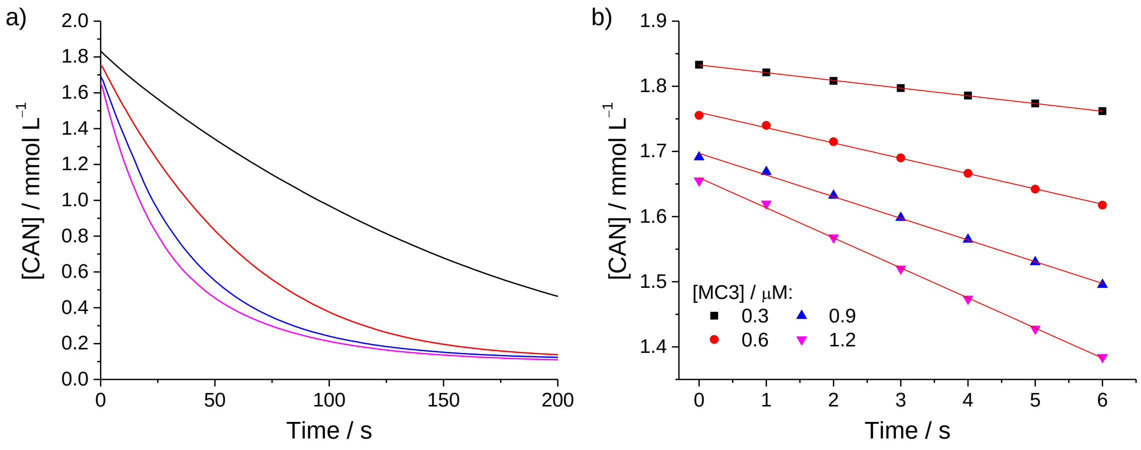

Figure S44. CAN absorbance decay at 360 nm depending on different **MC3** concentrations over 200 s (a), and between 0 and 6 s (b). Conditions: [CAN] = 2.0 mM in 2.0 mL 1:1 CH_3CN/H_2O (pH 1) at 25 °C.

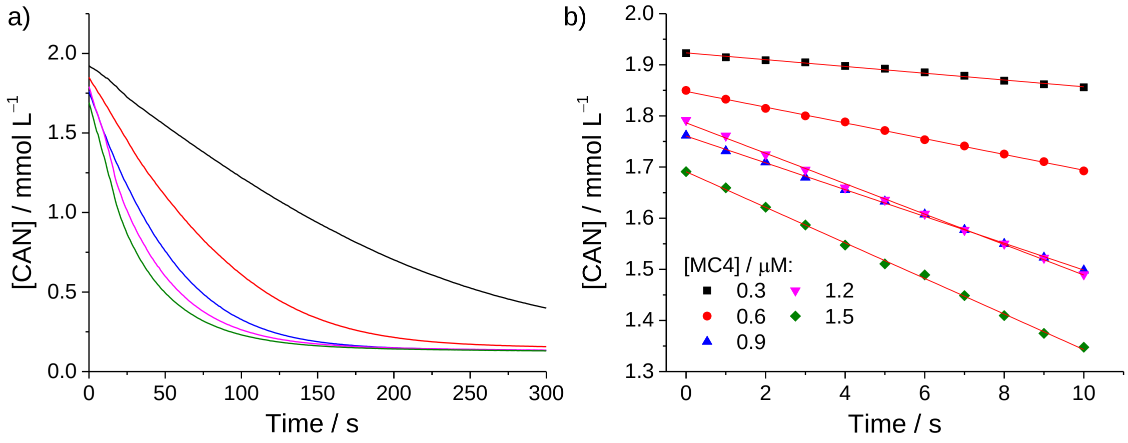

Figure S45. CAN absorbance decay at 360 nm depending on different **MC4** concentrations over 300 s (a), and between 0 and 10 s (b). Conditions: [CAN] = 2.0 mM in 2.0 mL 1:1 CH_3CN/H_2O (pH 1) at 25 °C.

13. CAN consumption – Variation of CAN Concentration

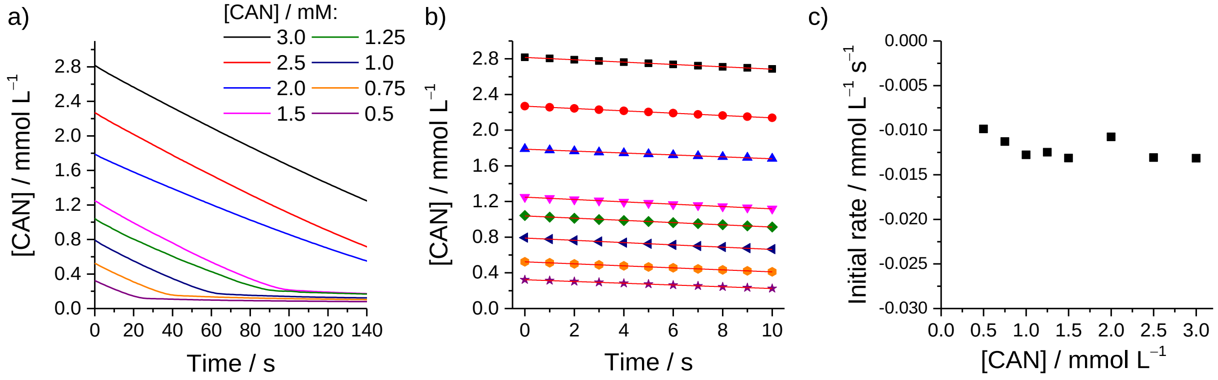

Figure S46. CAN absorbance decay at 360 nm, for [Ru(bda)(pic)$_2$] as catalyst, depending on different CAN concentrations over 140 s (a), and between 0 and 10 s (b) and the plot of the initial rates vs. the catalyst concentration (c). Conditions: [Ru(bda)(pic)$_2$] = 9.0 µM in 2.0 mL 1:1 CH_3CN/H_2O (pH 1) at 25 °C.

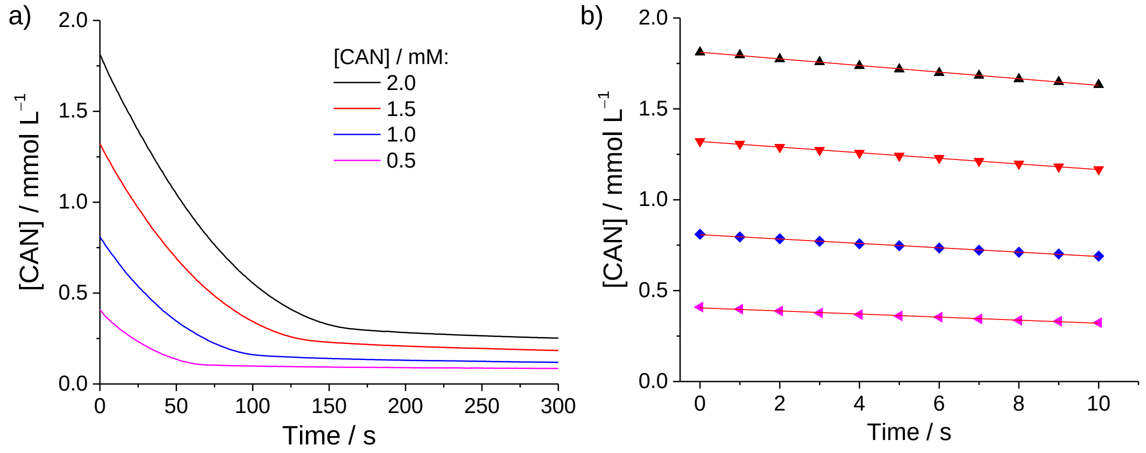

Figure S47. CAN absorbance decay at 360 nm depending on different CAN concentrations with **MC1** as catalyst over 300 s (a), and between 0 and 10 s (b). Conditions: [**MC1**] = 3.0 µM in 2.0 mL 1:1 CH_3CN/H_2O (pH 1) at 25 °C.

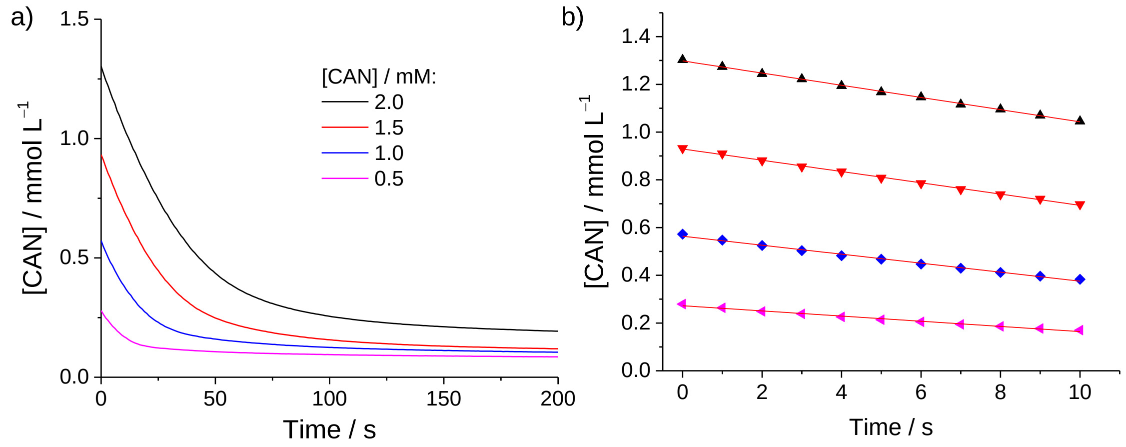

Figure S48. CAN absorbance decay at 360 nm depending on different CAN concentrations with **MC2** as catalyst over 200 s (a), and between 0 and 10 s (b). Conditions: [**MC2**] = 3.0 µM in 2.0 mL 1:1 CH_3CN/H_2O (pH 1) at 25 °C.

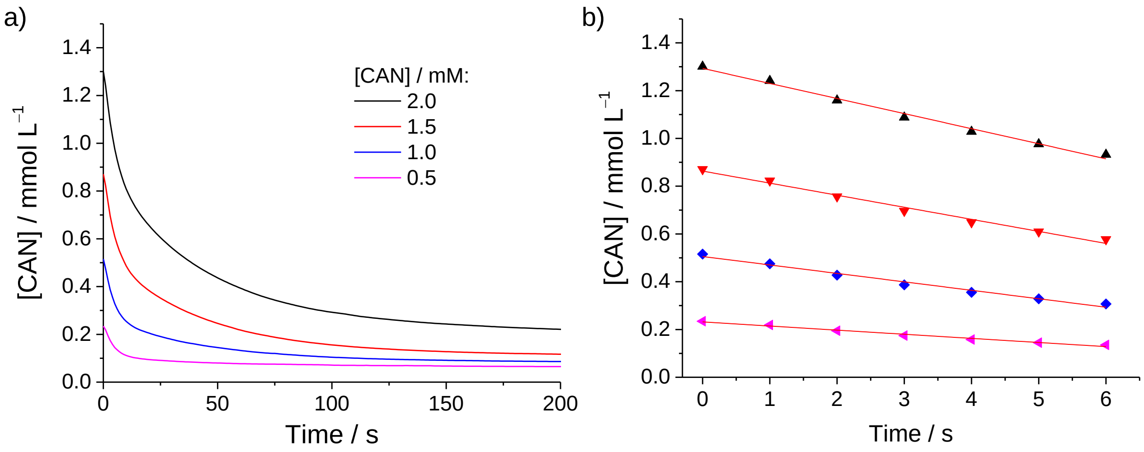

Figure S49. CAN absorbance decay at 360 nm depending on different CAN concentrations with **MC3** as catalyst over 200 s (a), and between 0 and 6 s (b). Conditions: [**MC3**] = 3.0 µM in 2.0 mL 1:1 CH_3CN/H_2O (pH 1) at 25 °C.

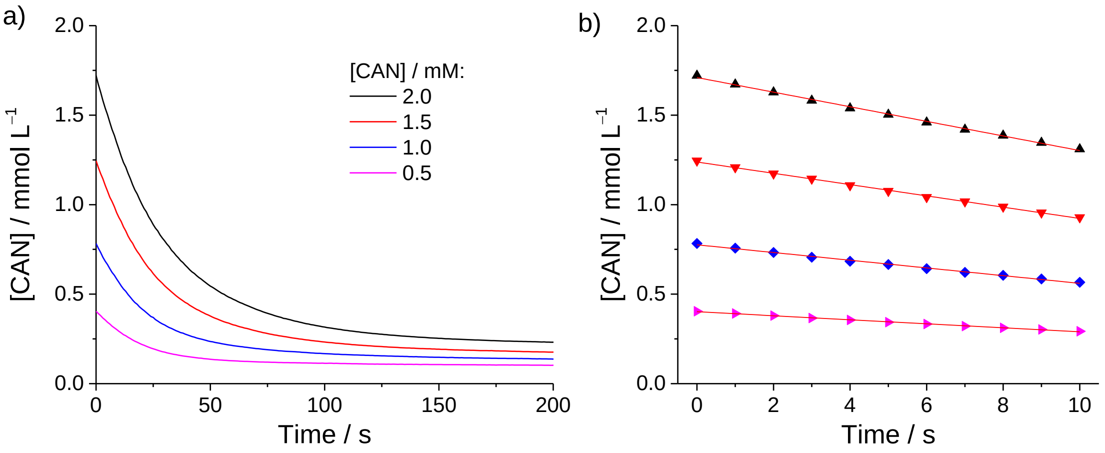

Figure S50. CAN absorbance decay at 360 nm depending on different CAN concentrations with **MC4** as catalyst over 150 s (a), and between 0 and 10 s (b). Conditions: [**MC4**] = 3.0 µM in 2.0 mL 1:1 CH_3CN/H_2O (pH 1) at 25 °C.

14. UV/Vis Redox Titration

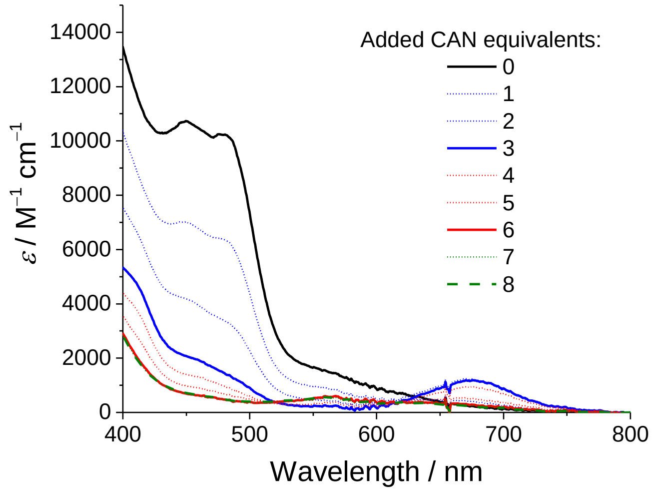

Figure S51. UV/Vis spectra of **MC1** (10^{-4} M in 1:1 CH_3CN/H_2O (pH 1, acid: CF_3SO_3H)) after the successive addition of CAN equivalents.

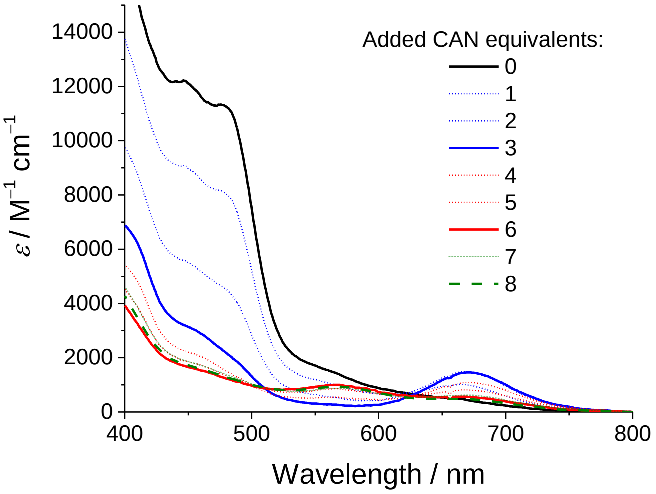

Figure S52. UV/Vis spectra of **MC2** (10^{-4} M in 1:1 CH_3CN/H_2O (pH 1, acid: CF_3SO_3H)) after the successive addition of CAN equivalents.

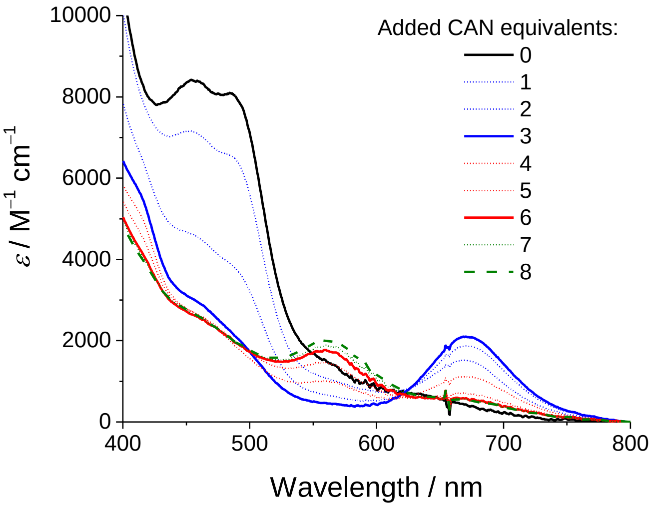

Figure S53. UV/Vis spectra of **MC3** (10^{-4} M in 1:1 CH_3CN/H_2O (pH 1, acid: CF_3SO_3H)) after the successive addition of CAN equivalents.

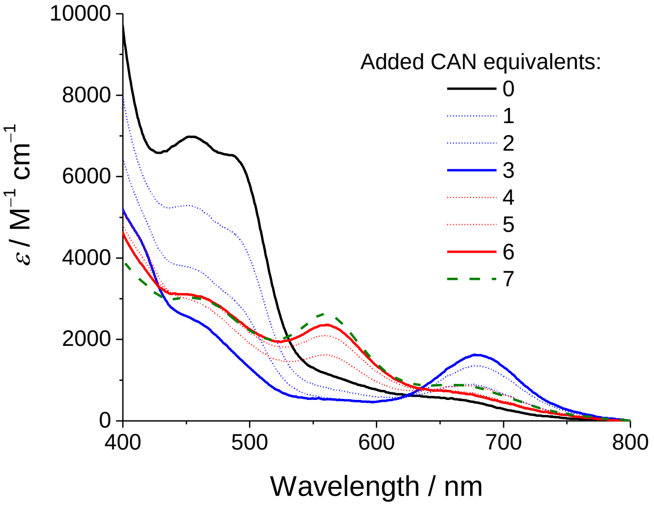

Figure S54. UV/Vis spectra of **MC4** (10^{-4} M in 1:1 CH_3CN/H_2O (pH 1, acid: CF_3SO_3H)) after the successive addition of CAN equivalents.

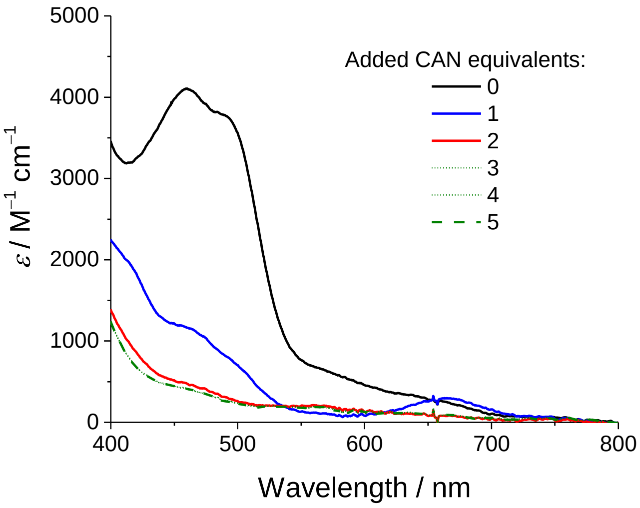

Figure 55. UV/Vis spectra of [Ru(bda)(pic)$_2$] (10^{-4} M in 1:1 CH_3CN/H_2O (pH 1, acid: CF_3SO_3H)) after the successive addition of CAN equivalents.

15. Stability Tests

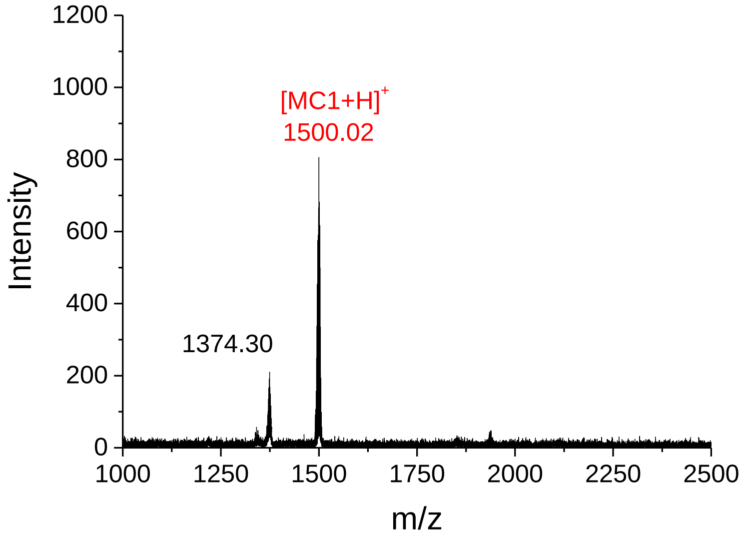

Figure S56. MALDI mass spectrum of **MC1** after 33 catalytic cycles (after the reduction with ascorbic acid).

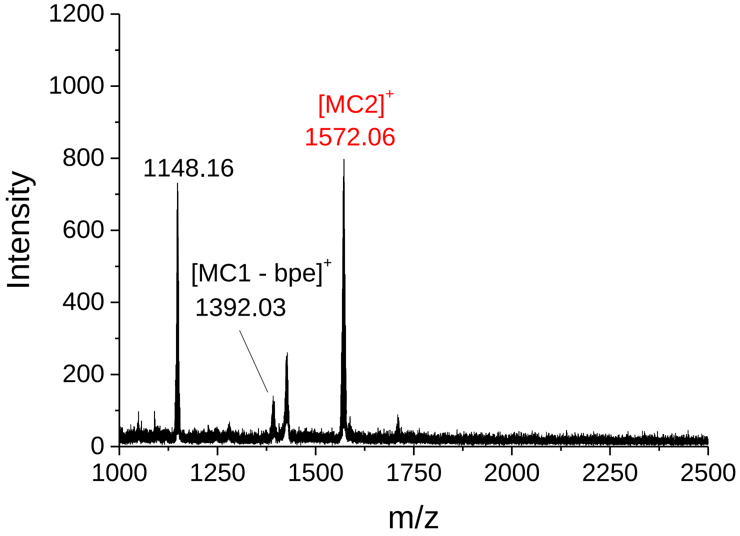

Figure S57. MALDI mass spectrum of **MC2** after 33 catalytic cycles (after the reduction with ascorbic acid).

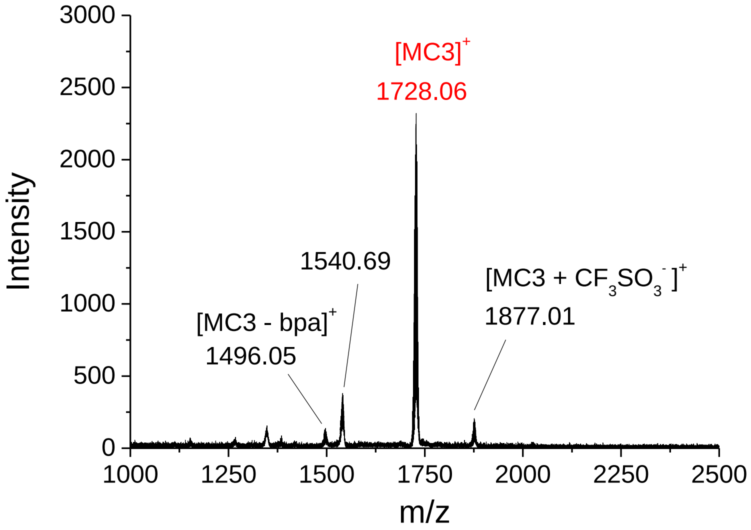

Figure S58. MALDI mass spectrum of **MC3** after 33 catalytic cycles (after the reduction with ascorbic acid).

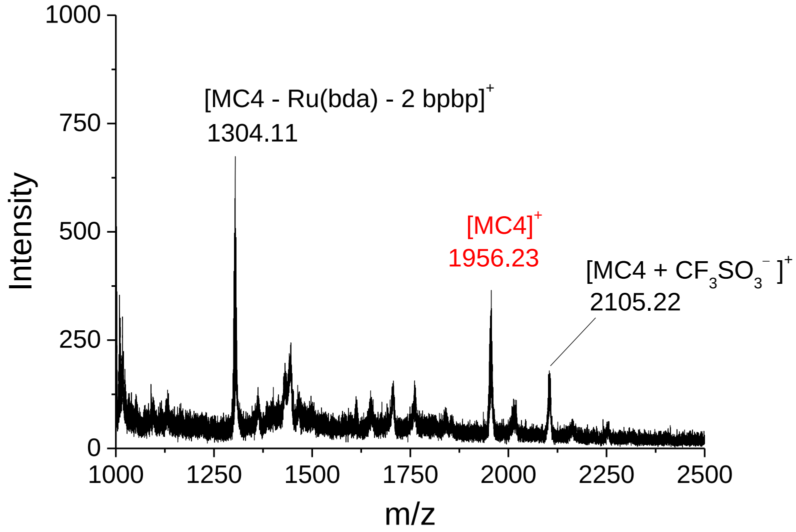

Figure S59. MALDI mass spectrum of **MC4** after 33 catalytic cycles (after the reduction with ascorbic acid).

16. Kinetic Isotope Effects

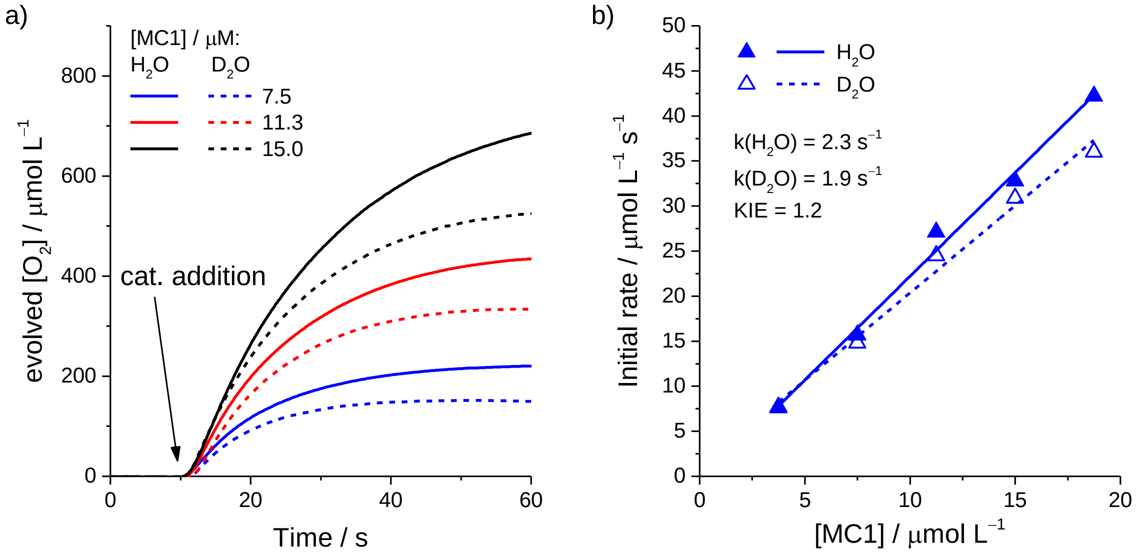

Figure S60. (a) Oxygen evolution vs. time during water oxidation with **MC1** as catalyst at varying catalyst concentrations in 2.0 mL aqueous pH 1 solutions (H_2O or D_2O) with 50% CH_3CN (v/v) as co-solvent using CAN (0.525M) as sacrificial oxidant. Measured with a Clark-type electrode set-up at 20 °C. (b) Plot of initial catalytic rates vs. **MC1** concentration, with corresponding linear regression fits to determine reaction rates k(H_2O) and k(D_2O).

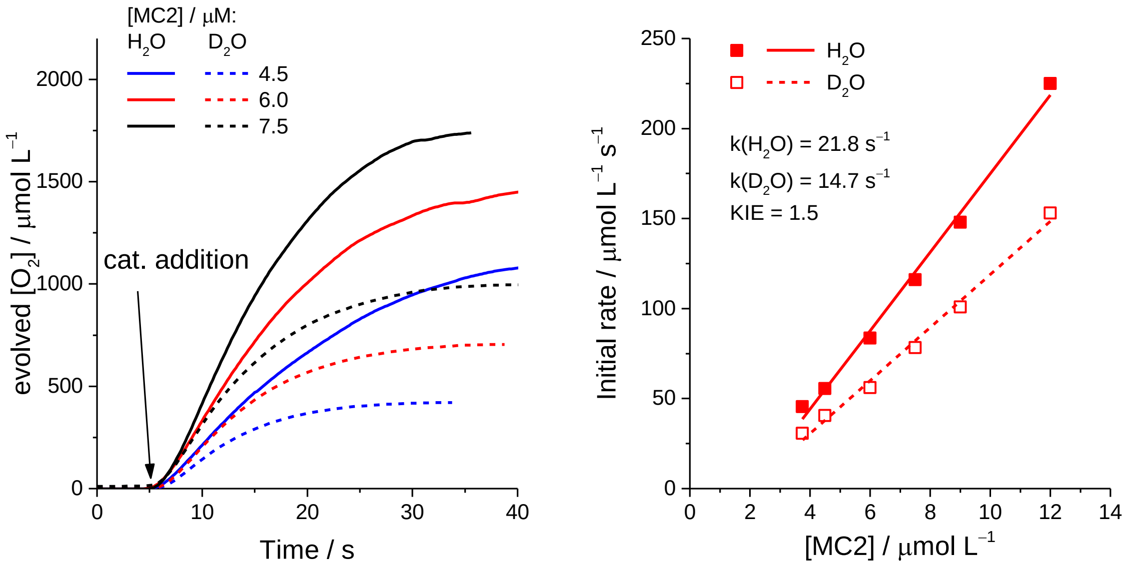

Figure S61. (a) Oxygen evolution vs. time during water oxidation with **MC2** as catalyst at varying catalyst concentrations in 2.0 mL aqueous pH 1 solutions (H_2O or D_2O) with 50% CH_3CN (v/v) as co-solvent using CAN (0.525M) as sacrificial oxidant. Measured with a Clark-type electrode set-up at 20 °C. (b) Plot of initial catalytic rates vs. **MC2** concentration, with corresponding linear regression fits to determine reaction rates k(H_2O) and k(D_2O).

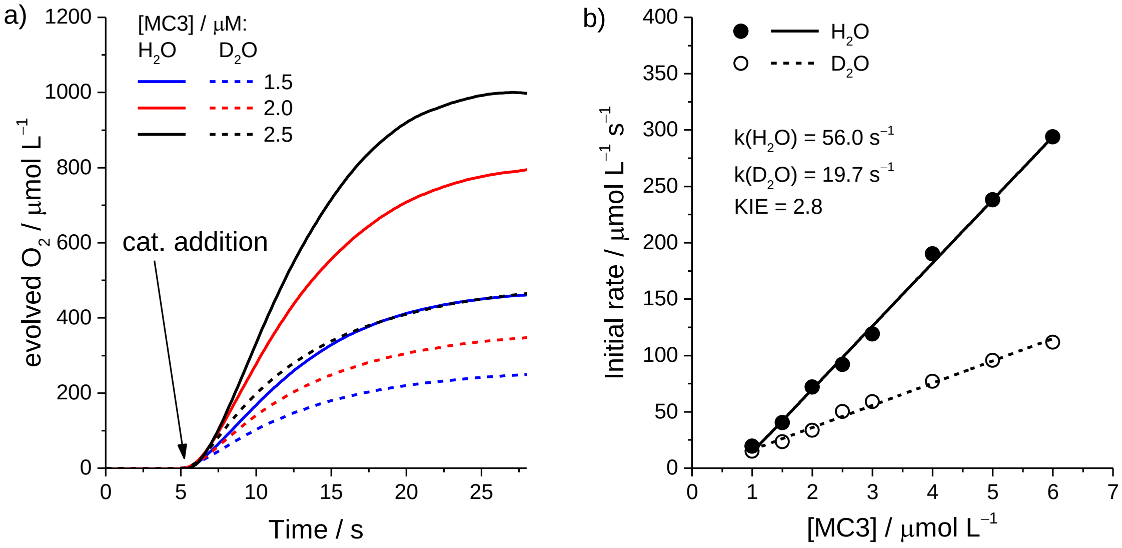

Figure S62. (a) Oxygen evolution vs. time during water oxidation with **MC3** as catalyst at varying catalyst concentrations in 2.0 mL aqueous pH 1 solutions (H_2O or D_2O) with 50% CH_3CN (v/v) as co-solvent using CAN (0.525M) as sacrificial oxidant. Measured with a Clark-type electrode set-up at 20 °C. (b) Plot of initial catalytic rates vs. **MC3** concentration, with corresponding linear regression fits to determine reaction rates k(H_2O) and k(D_2O).

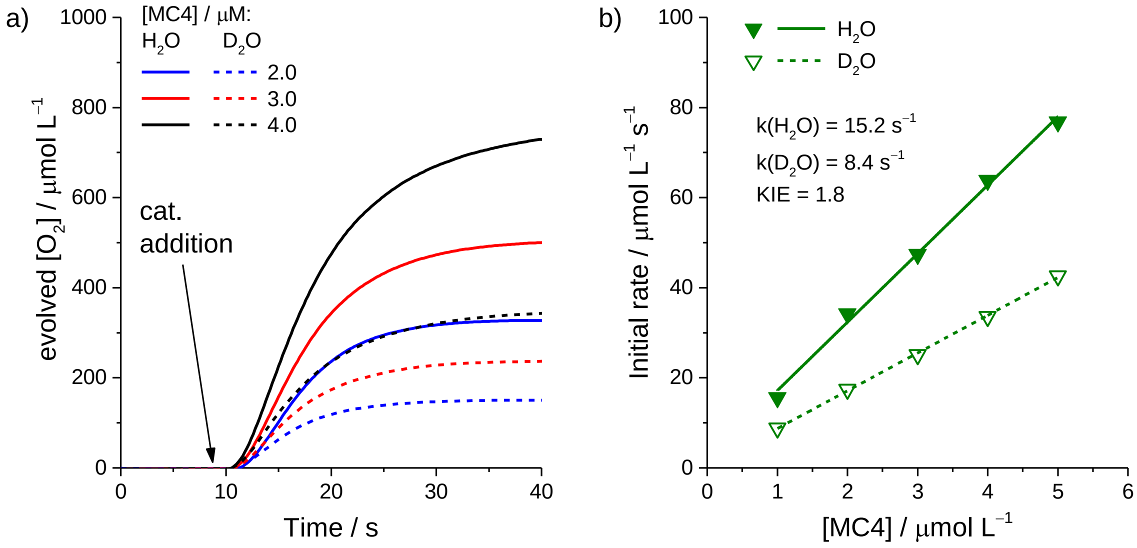

Figure S63. (a) Oxygen evolution vs. time during water oxidation with **MC4** as catalyst at varying catalyst concentrations in 2.0 mL aqueous pH 1 solutions (H_2O or D_2O) with 50% CH_3CN (v/v) as co-solvent using CAN (0.525M) as sacrificial oxidant. Measured with a Clark-type electrode set-up at 20 °C. (b) Plot of initial catalytic rates vs. **MC4** concentration, with corresponding linear regression fits to determine reaction rates k(H_2O) and k(D_2O).

17. Mechanistic Investigations by Molecular Dynamics Simulations

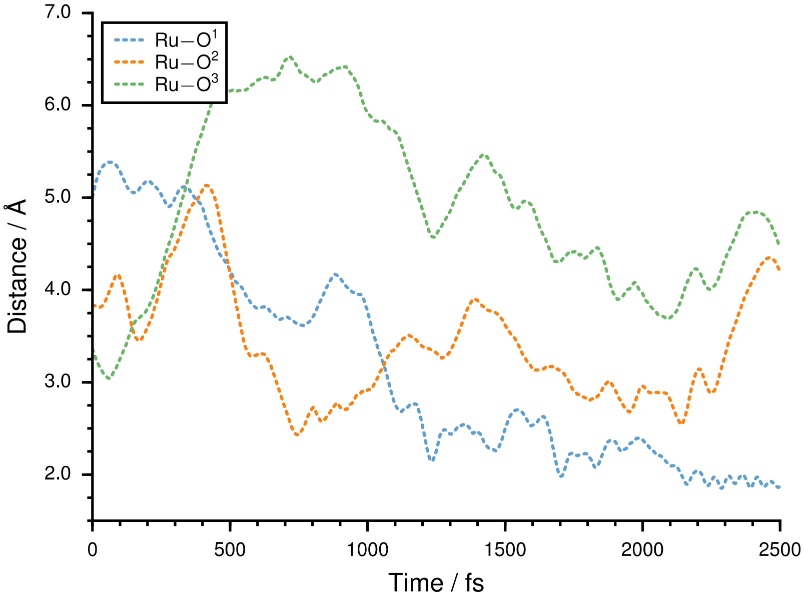

Figure S64. Results from the oxidation simulation from Ru^{II} to Ru^{III} for **MC3**. Depicted are the Ru–O distances from each Ru atom to the respective closest water molecule.

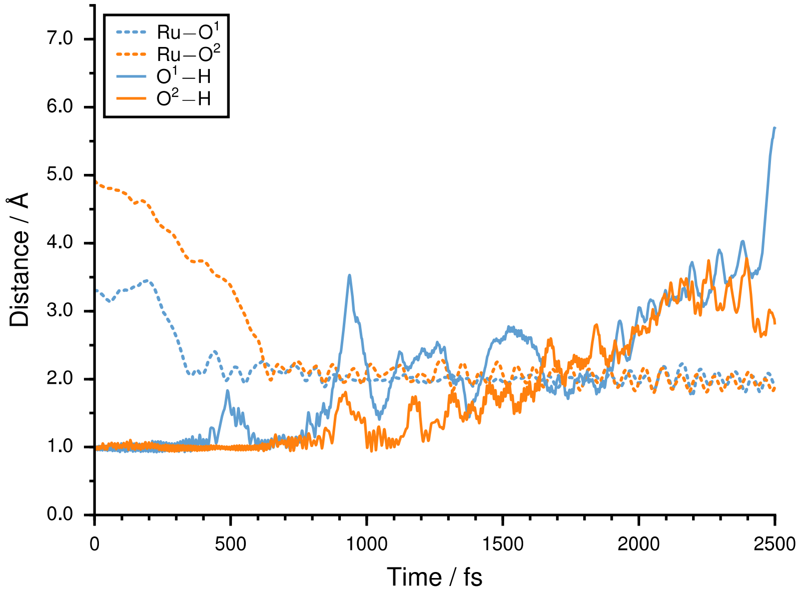

Figure S65. Results from the oxidation simulation from Ru^{III} to Ru^{IV} for **MC3**. Depicted are the Ru–O distances from each reacting Ru atom to the respective closest water molecule, as well as the O–H distances that are elongated during the propagation.

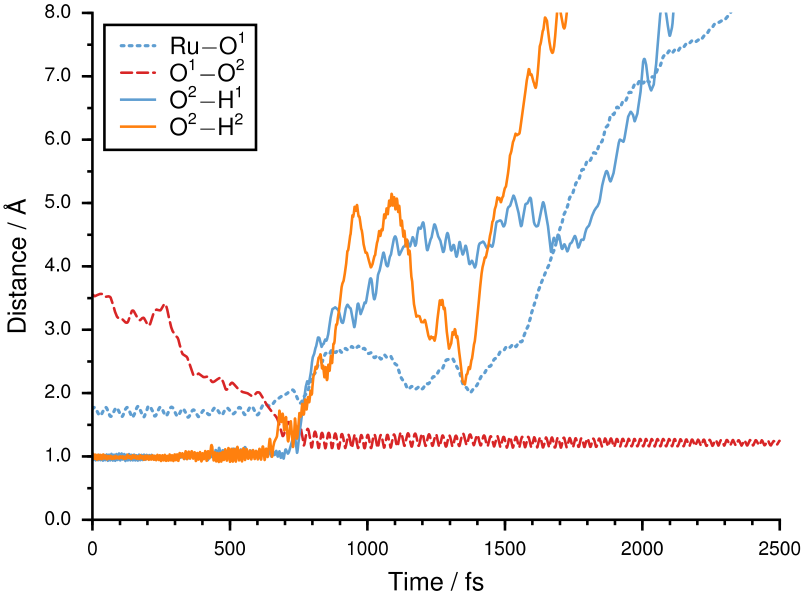

Figure S66. Results from the oxidation simulation from Ru^{V} with subsequent O−O bond formation for **MC3**. The electronic state was switched from singlet to triplet after 672 fs. Depicted are the Ru–O, O–O and O–H distances of the atoms that are involved in the reaction.

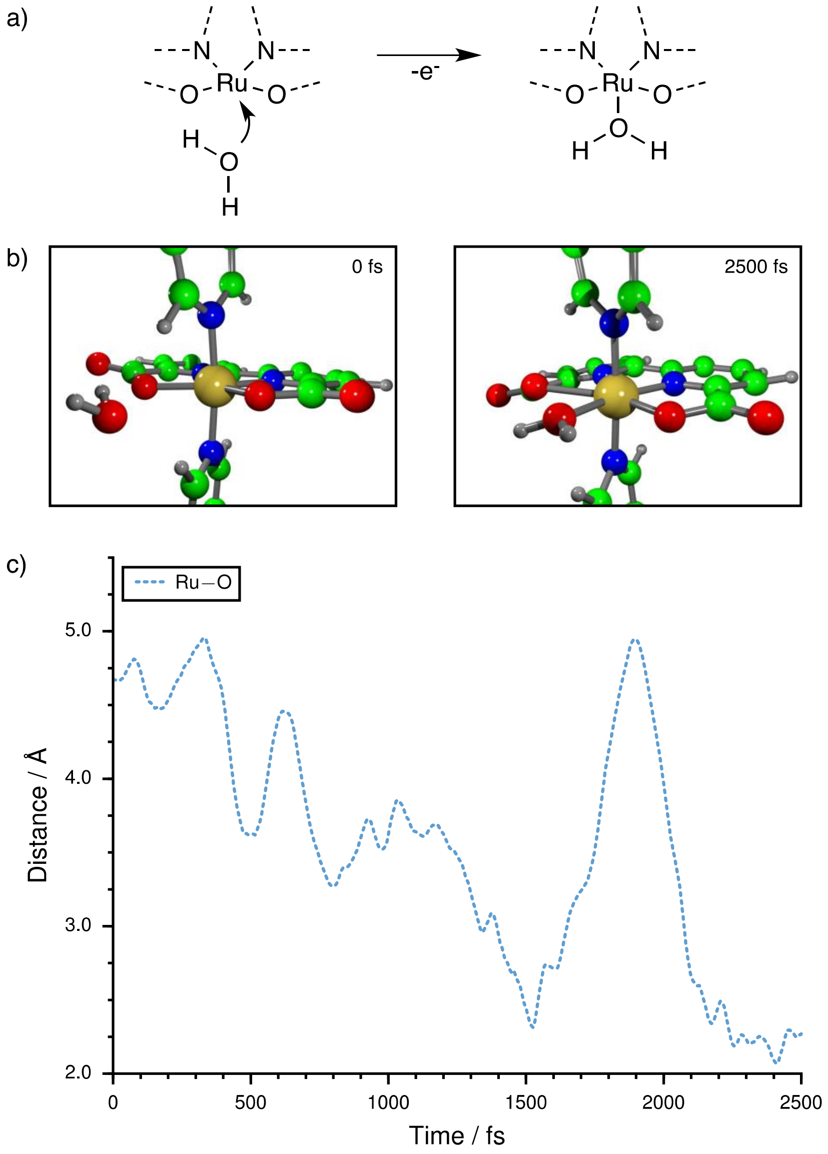

Figure S67. Results from the oxidation simulation from Ru^{II} to Ru^{III} for [Ru(bda)(pic)$_2$]. In addition to (a) the reaction scheme and (b) the corresponding structures from the MD simulation, the Ru–O distance to the water molecule is depicted in (c). For the sake of clarity, additional solvent molecules are omitted in (b). (green = carbon, grey = hydrogen, red = oxygen, blue = nitrogen, yellow = ruthenium)

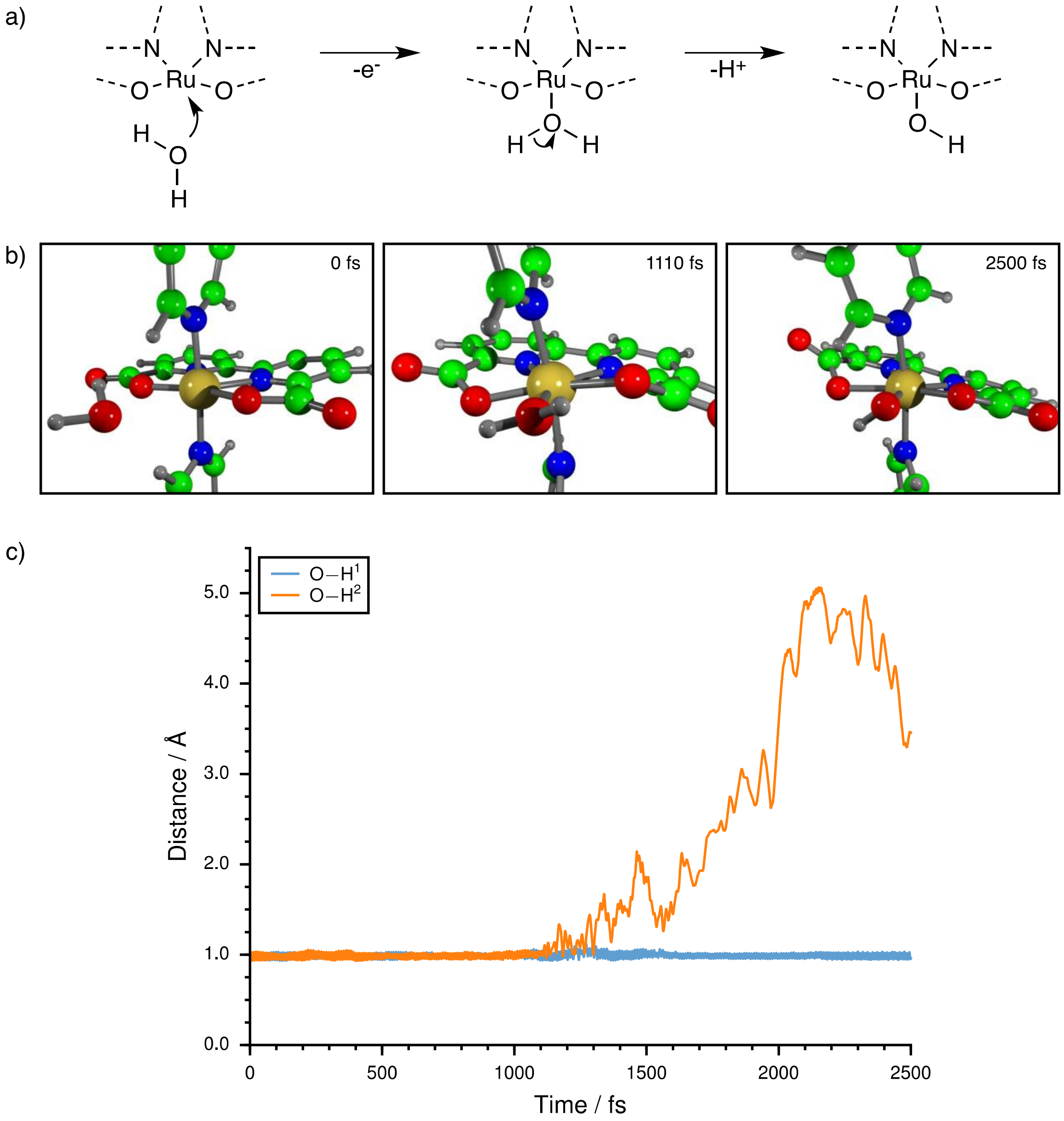

Figure S68. Results from the oxidation simulation from Ru^{III} to Ru^{IV} for $[Ru(bda)(pic)_2]$. In addition to (a) the reaction scheme and (b) the corresponding structures from the MD simulation, the O–H^1 and O–H^2 distances within the coordinating water molecule are depicted in (c). For the sake of clarity, additional solvent molecules are omitted in (b). (green = carbon, grey = hydrogen, red = oxygen, blue = nitrogen, yellow = ruthenium)

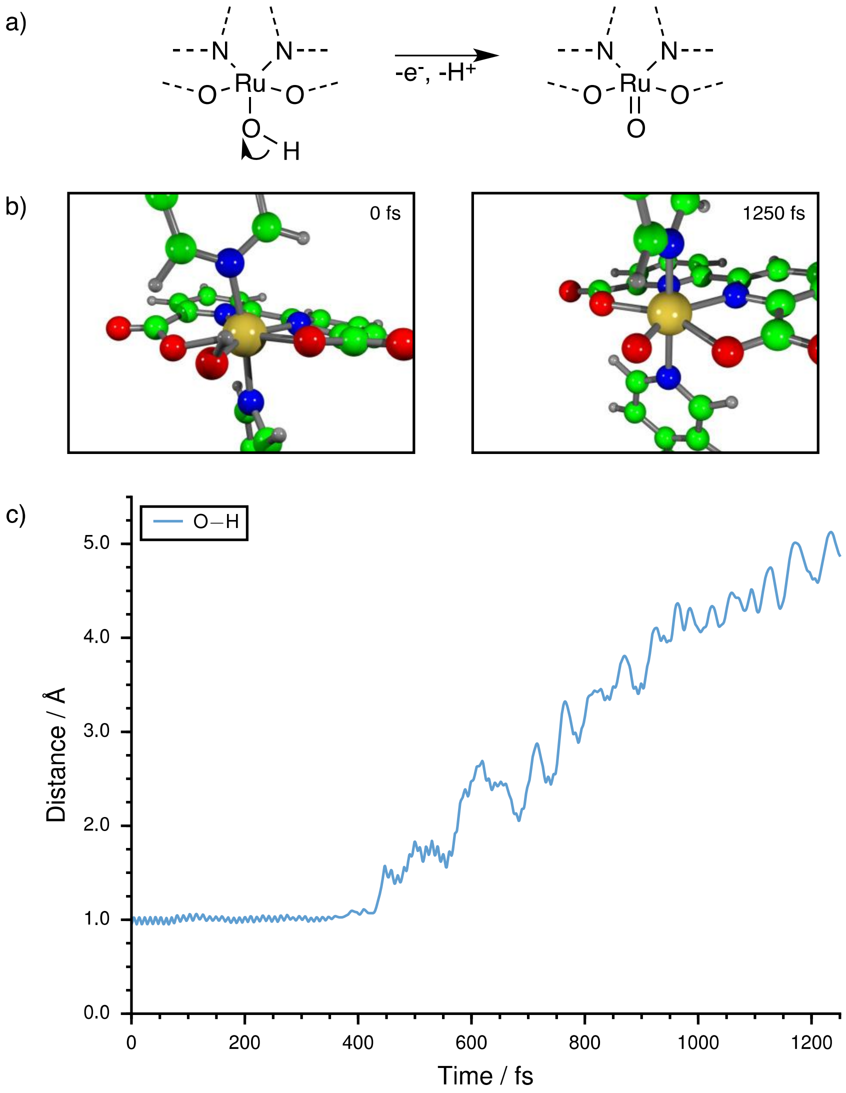

Figure S69. Results from the oxidation simulation from Ru^{IV} to Ru^{V} for $[Ru(bda)(pic)_2]$. In addition to (a) the reaction scheme and (b) the corresponding structures from the MD simulation, the O–H distance of the OH-ligand is depicted in (c). For the sake of clarity, additional solvent molecules are omitted in (b). (green = carbon, grey = hydrogen, red = oxygen, blue = nitrogen, yellow = ruthenium)

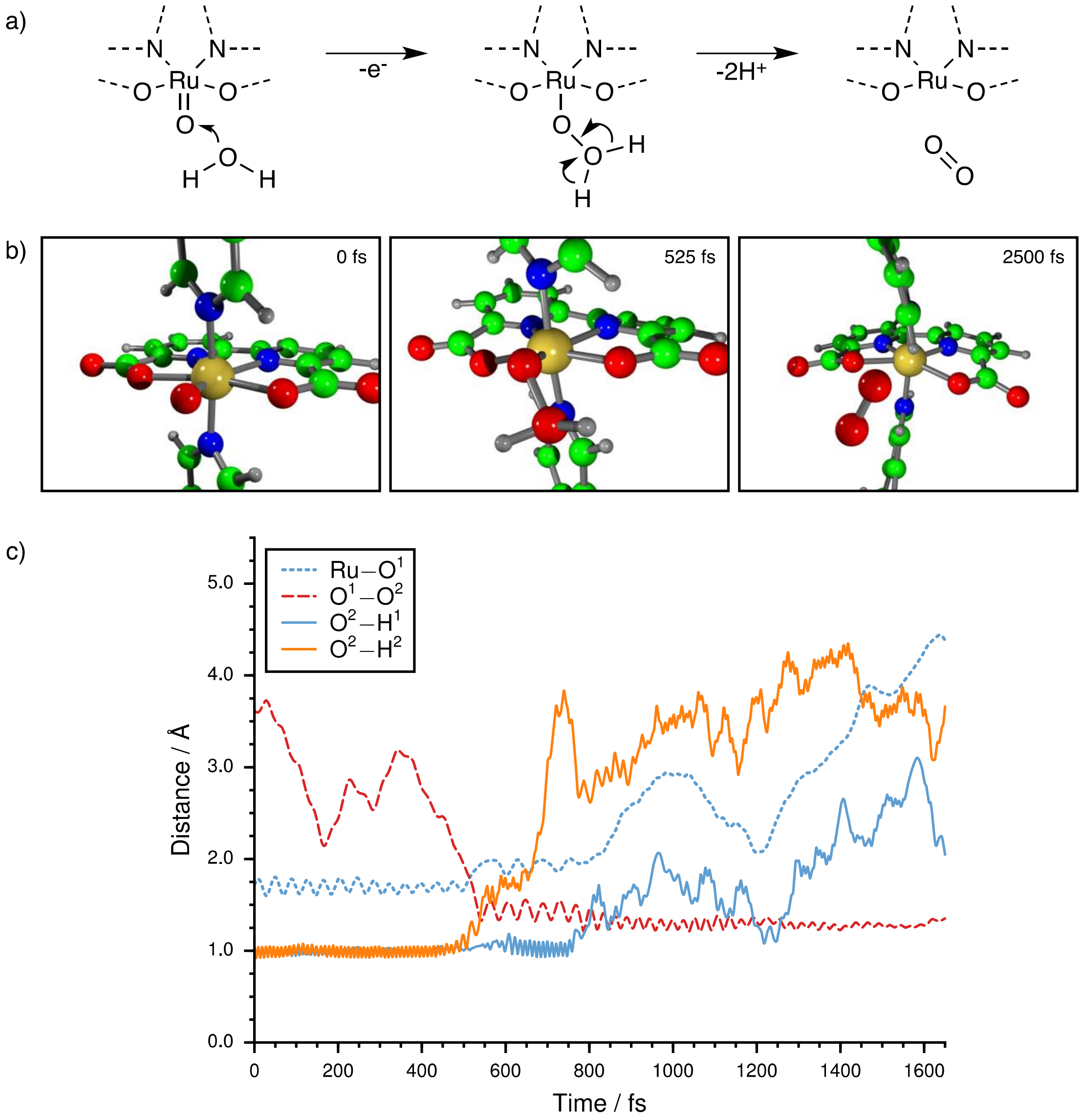

Figure S70. Results from the oxidation simulation from Ru^V with subsequent O–O bond formation for [Ru(bda)(pic)$_2$]. The electronic state was switched from singlet to triplet after 525 fs. In addition to (a) the reaction scheme and (b) the corresponding structures from the MD simulation, the Ru–O^1 distance, the O^1–O^2 distance of the evolving bond and both the O^2–H distances are depicted in (c). For the sake of clarity, additional solvent molecules are omitted in (b). (green = carbon, grey = hydrogen, red = oxygen, blue = nitrogen, yellow = ruthenium)

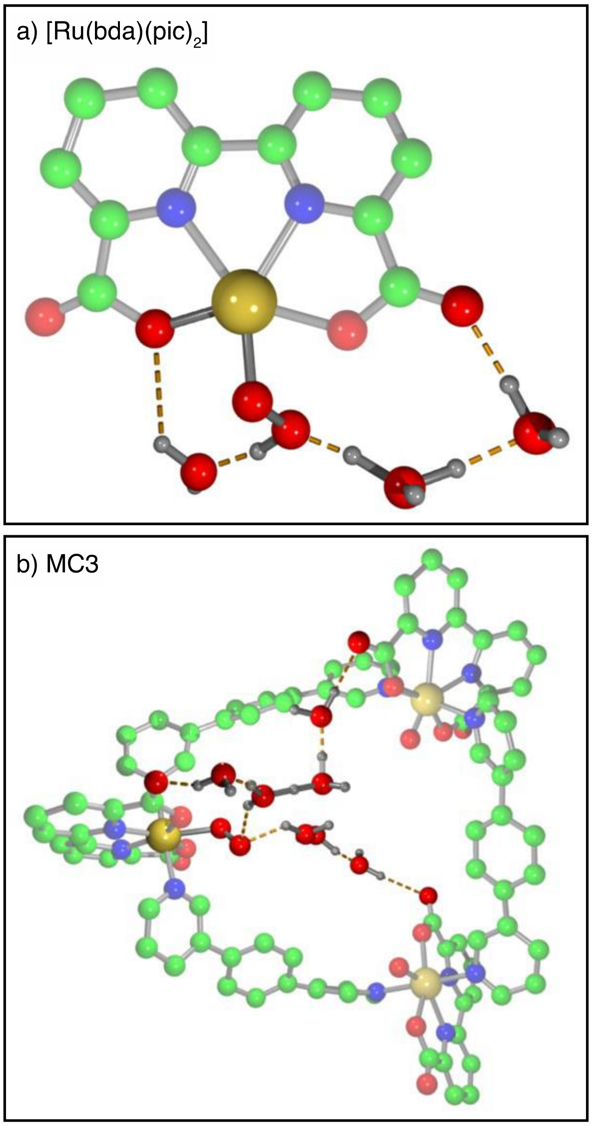

Figure S71. Depiction of hydrogen bonding networks in the O–O bond formation step after the first proton abstraction in (a) $[Ru(bda)(pic)_2]$ and (b) **MC3**. C-bound hydrogen atoms and pic-ligands are omitted for clarity. Only relevant water molecules are displayed. (green = carbon, grey = hydrogen, red = oxygen, blue = nitrogen, yellow = ruthenium)

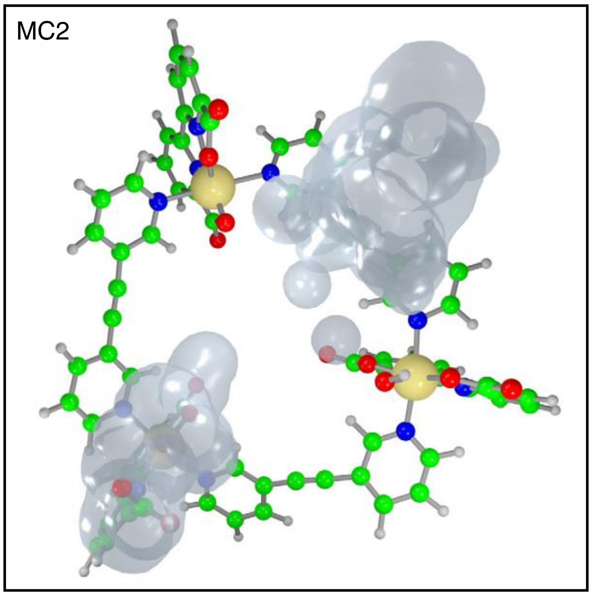

Figure S72. Dynamic proton delocalization cavities of **MC2** calculated based on the reaction MD from Ru^{IV} to Ru^{V} in the time interval from 0 to 1715 fs. The given structures are taken from the last simulation step. The solvent is not displayed for clarity. (green = carbon, grey = hydrogen, red = oxygen, blue = nitrogen, yellow = ruthenium)

18. References

1. L. Duan, A. Fischer, Y. Xu and L. Sun, *J. Am. Chem. Soc.*, 2009, **131**, 10397-10399.
2. D. K. Chand, K. Biradha, M. Kawano, S. Sakamoto, K. Yamaguchi and M. Fujita, *Chem. - Asian J.*, 2006, **1**, 82-90.
3. K. Park, G. Bae, J. Moon, J. Choe, K. H. Song and S. Lee, *J. Org. Chem.*, 2010, **75**, 6244-6251.
4. M. Schulze, V. Kunz, P. D. Frischmann and F. Würthner, *Nature Chem.*, 2016, **8**, 576-583.
5. G. Sheldrick, *Acta Crystallogr.*, *Sect. A*, 2008, **64**, 112-122.
6. A. Spek, *Acta Crystallogr.*, *Sect. A*, 1990, **46**, c34.
7. J. P. Perdew, K. Burke and M. Ernzerhof, *Phys. Rev. Lett.*, 1996, **77**, 3865-3868.
8. F. Weigend and R. Ahlrichs, *Phys. Chem. Chem. Phys.*, 2005, **7**, 3297-3305.
9. D. Andrae, U. Häußermann, M. Dolg, H. Stoll and H. Preuß, *Theor. Chim. Acta*, 1990, **77**, 123-141.
10. TURBOMOLE, V6.3, a development of University of Karlsruhe and Forschungszentrum Karlsruhe GmbH, 1989-2007, TURBOMOLE GmbH, since 2007; available from http://www.turbomole.com.
11. W. L. Jorgensen, J. Chandrasekhar, J. D. Madura, R. W. Impey and M. L. Klein, *J. Chem. Phys.*, 1983, **79**, 926-935.
12. J. W. Ponder and F. M. Richards, *J. Comput. Chem.*, 1987, **8**, 1016-1024.
13. W. L. Jorgensen, D. S. Maxwell and J. Tirado-Rives, *J. Am. Chem. Soc.*, 1996, **118**, 11225-11236.
14. A. K. Rappe, C. J. Casewit, K. S. Colwell, W. A. Goddard and W. M. Skiff, *J. Am. Chem. Soc.*, 1992, **114**, 10024-10035.
15. T. Yanai, D. P. Tew and N. C. Handy, *Chem. Phys. Lett.*, 2004, **393**, 51-57.
16. M. J. Frisch, G. W. Trucks, H. B. Schlegel, G. E. Scuseria, M. A. Robb, J. R. Cheeseman, G. Scalmani, V. Barone, G. A. Petersson, H. Nakatsuji, X. Li, M. Caricato, A. Marenich, J. Bloino, B. G. Janesko, R. Gomperts, B. Mennucci, H. P. Hratchian, J. V. Ortiz, A. F. Izmaylov, J. L. Sonnenberg, D. Williams-Young, F. Ding, F. Lipparini, F. Egidi, J. Goings, B. Peng, A. Petrone, T. Henderson, D. Ranasinghe, V. G. Zakrzewski, J. Gao, N. Rega, G. Zheng, W. Liang, M. Hada, M. Ehara, K. Toyota, R. Fukuda, J. Hasegawa, M. Ishida, T. Nakajima, Y. Honda, O. Kitao, H. Nakai, T. Vreven, K. Throssell, J. A. M. Jr., J. E. Peralta, F. Ogliaro, M. Bearpark, J. J. Heyd, E. Brothers, K. N. Kudin, V. N. Staroverov, T. Keith, R. Kobayashi, J. Normand, K. Raghavachari, A. Rendell, J. C. Burant, S. S. Iyengar, J. Tomasi, M. Cossi, J. M. Millam, M. Klene, C. Adamo, R. Cammi, J. W. Ochterski, R. L. Martin, K. Morokuma, O. Farkas, J. B. Foresman and D. J. Fox, *Gaussian-09 Revision D.01. Gaussian Inc. Wallingford CT*, 2009.